

Mechanical and Thermophysical Properties of 3D-Printed SiC Before and After Neutron Irradiation – FY21



T.S. Byun
T.G. Lach
H. Wang
D.A. Collins
A.G. Le Coq
K.D. Linton
et al.

May 2021

M2TC-21OR0403022

**Approved for public release.
Distribution is unlimited.**



DOCUMENT AVAILABILITY

Reports produced after January 1, 1996, are generally available free via US Department of Energy (DOE) SciTech Connect.

Website www.osti.gov

Reports produced before January 1, 1996, may be purchased by members of the public from the following source:

National Technical Information Service
5285 Port Royal Road
Springfield, VA 22161
Telephone 703-605-6000 (1-800-553-6847)
TDD 703-487-4639
Fax 703-605-6900
E-mail info@ntis.gov
Website <http://classic.ntis.gov/>

Reports are available to DOE employees, DOE contractors, Energy Technology Data Exchange representatives, and International Nuclear Information System representatives from the following source:

Office of Scientific and Technical Information
PO Box 62
Oak Ridge, TN 37831
Telephone 865-576-8401
Fax 865-576-5728
E-mail reports@osti.gov
Website <https://www.osti.gov/>

This report was prepared as an account of work sponsored by an agency of the United States Government. Neither the United States Government nor any agency thereof, nor any of their employees, makes any warranty, express or implied, or assumes any legal liability or responsibility for the accuracy, completeness, or usefulness of any information, apparatus, product, or process disclosed, or represents that its use would not infringe privately owned rights. Reference herein to any specific commercial product, process, or service by trade name, trademark, manufacturer, or otherwise, does not necessarily constitute or imply its endorsement, recommendation, or favoring by the United States Government or any agency thereof. The views and opinions of authors expressed herein do not necessarily state or reflect those of the United States Government or any agency thereof.

Transformational Challenge Reactor Program

**MECHANICAL AND THERMOPHYSICAL PROPERTIES OF 3D-PRINTED SiC
BEFORE AND AFTER NEUTRON IRRADIATION – FY 2021**

T.S. Byun
T.G. Lach
C.M. Parish
H. Wang
A.A. Trofimov
D.A. Collins
A.G. Le Coq
K.D. Linton
M.D. Richardson
B.C. Jolly
M.P. Trammell
A.T. Schumacher
G. Vasudevamurthy
T. Koyanagi
K.A. Terrani

May 2021

M2TC-21OR0403022

Prepared by
OAK RIDGE NATIONAL LABORATORY
Oak Ridge, TN 37831-6283
managed by
UT-BATTELLE, LLC
for the
US DEPARTMENT OF ENERGY
under contract DE-AC05-00OR22725

CONTENTS

FIGURES	v
TABLES	vi
ABBREVIATIONS	viii
SUMMARY	ix
1. INTRODUCTION	1
1.1 BACKGROUND	1
1.2 PERFORMED WORK	2
1.3 PURPOSE OF DOCUMENT	2
2. MATERIALS AND SPECIMENS	3
2.1 A COMBINED PROCESS OF BINDERJET PRINTING AND CVI.....	3
2.2 SiC SPECIMENS AND CONFIGURATIONS	3
3. BASELINE TESTING AND CHARACTERIZATION	5
3.1 FAILURE STRENGTH OF 3D-PRINTED SiC.....	5
3.1.1 Equibiaxial Flexural Strength Test	5
3.1.2 Statistical Treatment of Failure Strength Data.....	6
3.1.3 Baseline Failure Strength Data for 3D-Printed SiC	7
3.1.4 Cause of Variation in Failure Strength of SiC	8
3.2 THERMOPHYSICAL PROPERTIES OF 3D-PRINTED SiC.....	10
3.2.1 Thermal Diffusivity	10
3.2.2 Density Evaluation.....	12
3.2.3 Specific Heat Capacity.....	13
3.2.4 Thermal Conductivity	14
3.2.5 Coefficient of Thermal Expansion.....	15
3.2.6 Elastic Constants and Density Measured by Resonant Ultrasound Spectroscopy	16
4. NEUTRON IRRADIATION	18
4.1 IRRADIATION PLAN AND CAPSULE DESIGN	18
4.2 POST-IRRADIATION TREATMENT	20
5. POST-IRRADIATION EXAMINATION AND PROPERTIES.....	21
5.1 FAILURE STRENGTH AND STATISTICAL BEHAVIOR	21
5.2 THERMOPHYSICAL PROPERTIES.....	22
5.3 MICROSTRUCTURE AFTER IRRADIATION	25
5.3.1 Neutron Irradiation Effects	25
5.3.2 Ion Irradiation Effects.....	27
6. SUMMARY AND CONCLUSIONS	28
7. REFERENCES	30

FIGURES

Figure 1. Schematic of orientation relationship in binderjet printing [20]: sample orientation on powder bed during binderjet printing, with the build progress indicated in the Z direction, stacking and fusing successive XY powder planes.....	4
Figure 2. Porous morphology of 3D-printed SiC: (a) low magnification and (b) high magnification optical image of cross section of a poorly infiltrated XY disk, and (c) cross section of an optimally infiltrated XY disk.	5
Figure 3. Schematic section view of fixturing and test specimen for equibiaxial flexural strength testing.....	6
Figure 4. Weibull plots of SiC failure strength data from equibiaxial flexural strength testing.....	8
Figure 5. Weibull plots of SiC failure strength data from equibiaxial flexural strength testing with two different thicknesses and surface conditions.....	9
Figure 6. Laser flash system for thermal diffusivity (left), differential scanning calorimeter (DSC) for specific heat (C_p) (center), and CTE (right) testing systems.....	10
Figure 7. Thermal diffusivity of 3D-printed SiC after CVI.....	11
Figure 8. Density of 3D-printed SiC after CVI and CVD SiC.....	12
Figure 9. C_p vs. temperature plots of three 3D-printed SiC samples during heating and cooling (SiC Handbook values are represented by the dashed red line).....	13
Figure 10. C_p (curve-fitting of heating data) in three printing directions compared with the reference data (Eq. (10) in the SiC Handbook [8]).....	14
Figure 11. Thermal diffusivity and calculated thermal conductivity of three 3D-printed SiC samples with different orientation.	14
Figure 12. Coefficient of thermal expansion (CTE) vs. temperature for nine 3D-printed SiC samples.....	15
Figure 13. Examples of RUS spectra from the samples 20200331-2-3 #3 (2 nd and 3 rd spectra), #5 (4 th and 5 th spectra), #7 (bottom two spectra). Peak 1.....	16
Figure 14. Elastic constants and density of 3D-printed SiC with XY orientation: (a) Young's modulus, (b) Poisson's ratio, and (c) density.....	17
Figure 15. Rabbit capsule design for irradiation of SiC disk specimens.	19
Figure 16. Parts layout for the capsule SDTR01 showing 32 SiC disk specimens, 8 temperature monitors, and other capsule structural and support components.	19
Figure 17. Disk specimens recovered after hot cell disassembly of capsule SDTR05 (showing 16 of the 32 disks from the capsule).....	20
Figure 18. Weibull plot of strength as determined from equiaxial ring-on-ring tests of 3D-printed SiC disks with XY and Z orientations before and after irradiation to 2.3 dpa.....	21
Figure 19. Thermal conductivity of 3D-printed SiC in the XY and Z orientations before and after irradiation to 2.3 dpa at various temperatures.....	23
Figure 20. Irradiation defect resistivity, R_d , as a function of irradiation temperature for 3D-printed SiC, CVD-SiC [8], and NITE-SiC [1].....	24
Figure 21. STEM BF and annular dark field images of the interface between the CVI matrix and the α -SiC particle after neutron irradiation in HFIR to a dose of 2.3 dpa at nominal temperatures of 400, 650, and 900°C.....	26
Figure 22. TEM BF images of the interface between the CVI matrix and α -SiC particles in the 5 MeV Si ion-irradiated specimens to a peak dose of 40 dpa at 350 and 650 °C.....	27
Figure 23. (a) Sample STEM-EELS spectrum highlighting position of plasmon peak relative to the zero-loss peak.....	28

TABLES

Table 1. Summary of SiC specimen builds for testing and evaluation, listing all specimens built by a combined binderjet printing and CVI process since 2019	4
Table 2. Summary result of Weibull statistics analysis for equibiaxial flexural strength tests.....	8
Table 3. Summary result of Weibull statistics analysis for equibiaxial flexural strength tests.....	10
Table 4. Curve fitting parameters in the thermal diffusivity equation for the XS, XY, and Z series specimens.....	12
Table 5. Loading of SiC disk specimens in irradiation experiment.....	18
Table 6. Irradiation test matrix for SiC disk specimens determined after irradiation.....	20
Table 7. Characteristic strength and Weibull modulus determined for 3D-printed SiC at different orientations before and after irradiation.....	22

ABBREVIATIONS

ADF	annular dark field
ASTM	American Society for Testing and Materials
BF	bright field
CTE	coefficient of thermal expansion
CVD	chemical vapor deposition
CVI	chemical vapor infiltration
DOE	US Department of Energy
DSC	differential scanning calorimeter
EELS	electron energy loss spectroscopy
FIB	focused ion beam
HFIR	High Flux Isotope Reactor
HR	heating rate
LAMDA	Low Activation Materials Development and Analysis
MDF	Manufacturing Demonstration Facility
MTS	methyltrichlorosilane
NIST	National Institute of Standards Technology
NITE	nano-infiltration transient eutectic
ORNL	Oak Ridge National Laboratory
PIE	post-irradiation examination
RUS	resonant ultrasound spectroscopy
SiC	silicon carbide
STEM	scanning transmission electron microscopy
TCR	Transformational Challenge Reactor
TEM	transmission electron microscopy
TM	temperature monitor
TRISO	tristructural isotropic
UHP	ultra-high purity
UN	uranium nitride

SUMMARY

This report presents the mechanical and thermophysical properties of 3D-printed silicon carbide (SiC) before and after neutron irradiation. These properties have been evaluated to assess the SiC fuel matrix of the Transformational Challenge Reactor (TCR). The TCR fuel form consists of an additively manufactured SiC matrix and uranium nitride tristructural isotropic (UN TRISO) fuel particles. The fuel is manufactured through a newly established processing route that combines binderjet 3D printing, TRISO fuel particle loading, and chemical vapor infiltration (CVI). Because the fuel matrix is a primary component of the TCR core, and because its response to mechanical and thermal loads during operation is one of the most influential factors on the integrity of the TCR core, the testing and evaluation efforts have been focused on producing mechanical and thermophysical properties data for the binderjet/CVI SiC. This report contains the mechanical and thermophysical property data that has been accumulated so far in the program. The main addition for the fiscal year includes the results of post-irradiation mechanical testing and thermophysical property measurement and the new strength datasets from the ongoing size effect testing. Discussion is particularly focused on assessment of the 3D-printed SiC with irradiation-induced displacement damage. Baseline mechanical and thermophysical properties were measured from disk specimens that were printed in different orientations. Properties measured included equibiaxial flexural failure strength, elastic constants, thermal diffusivity and conductivity, density, and the coefficient of thermal expansion (CTE). Flexural failure strength datasets showed similar Weibull distributions, regardless of sample variants that include different printing orientations. The mean failure strengths of the 3D-printed SiC variants were in the range of 280–310 MPa, which is slightly lower than that of the chemical vapor deposition (CVD) SiC. Thermophysical test results showed that specific heat and thermal expansion are not sensitive to the build direction of SiC samples, whereas thermal conductivity is highly dependent on the build direction and can be correlated to the anisotropic character of the 3D-printed SiC. Neutron irradiation tests were carried out on the 3D-printed 6 mm diameter SiC disk specimens. Neutron irradiation was implemented up to 2.3 dpa over a temperature range of 360–880°C in the High Flux Isotope Reactor (HFIR) at Oak Ridge National Laboratory (ORNL). No significant degradation in strength was observed in the SiC after irradiations under various conditions and in different orientations. Anisotropy that had been observed in the thermal conductivity of 3D-printed SiC before irradiation vanished after irradiation because the irradiation defect resistivity became dominant and similarly accumulated in the samples regardless of their orientations. Electron microscopy of the microstructure after neutron irradiation showed distinct defect morphologies in the heterogeneous material, but no evidence was observed for irradiation-induced cracking or degradation in the microstructure.

1. INTRODUCTION

1.1 BACKGROUND

The fuel form to be used in the Transformational Challenge Reactor (TCR) consists of conventionally manufactured uranium nitride tristructural isotropic (UN-TRISO) fuel particles embedded in a 3D-printed silicon carbide (SiC) matrix [1-3]. The fabrication method begins with a low-density SiC capsule which is produced using binderjet additive manufacturing technology. The SiC capsule is filled with TRISO-coated fuel particles and is then densified with highly crystalline SiC in a chemical vapor infiltration (CVI) process. Performance of the SiC fuel matrix under irradiation [4] is particularly important, as it occupies the largest volume among the solid structures and must demonstrate good structural and thermal behaviors as a fuel matrix and structure, serve as an additional barrier to radionuclide release, and function as a heat transfer medium. A streamlined, novel methodology for the production of carbide ceramics was developed recently under the TCR program [1] and is being leveraged to produce the fuel matrix for the TCR core. However, the binderjet/CVI SiC materials produced by the new processing route must undergo detailed evaluation to inform high fidelity reactor design and analysis, as well as material qualification activities.

Many studies have demonstrated the excellent high-temperature properties of SiC materials, including high strength, creep resistance, and oxidation resistance [1-3]. In particular, the materials' high radiation tolerance makes the SiC materials optimal for some nuclear structural components [4]. In fact, SiC ceramic has been one of the most important nuclear materials, with its use dating back to the middle of the last century [5]. In general, the quality of SiC for nuclear power applications greatly depends on its purity, crystallinity, and grain boundary state [1, 2]. Several manufacturing techniques are used to produce high quality, high density SiC matrices, including chemical vapor deposition (CVD) [3], nano-infiltration transient eutectic (NITE) processing [1], and CVI [4] of high purity SiC, often on highly pure SiC substrates or fibers. The CVD SiC process is a bulk processing technique that produces highly pure SiC [5, 6]. The CVD process was chosen for TCR nuclear applications because it is highly pure, stoichiometric, and crystalline [7, 8]. These characteristics are crucial for attaining manageable swelling and for preventing degradation in strength under irradiation-induced displacement damage [9, 10]. SiC with these characteristics has proved to be almost immune to radiation-induced degradation up to doses of at least 100 dpa in the point defect saturation regime (~200–900°C) [11]. Moreover, since thermal creep is almost absent in SiC below 1,400°C [12] and irradiation creep is insignificant [13, 14], it is a highly promising material for use in advanced reactors to be operated in high temperature, high burnup regimes.

Although these essential properties were attainable through various synthesis methods, deployment of SiC into advanced reactors has remained a significant challenge, mainly because it is difficult to manufacture SiC into complex geometries. To address this geometry limitation, one of the various methodologies [16-21] is to combine binderjet printing and CVI to produce highly crystalline, stoichiometric, high purity SiC in a wide range of geometries [15]. Unlike sintering of generic SiC or the NITE process [1, 16, 17], the CVI process only requires a temperature of about 1,000–1,200°C and is thus considered a low-temperature process [4]. This is important for processing TCR fuel blocks with high precision because the dimensional distortion in an as-printed fuel basket is limited in this low-temperature regime. The additive manufacturing binderjet technology has been successfully combined with CVI at ORNL and is being used to manufacture the reflector and fuel elements for the TCR demonstration [5, 18]. One remaining issue with CVI processing may be the inherent porosity that arises from infiltration that prematurely closes off open pores, resulting in porosities as high as 20% in some fiber/matrix composites. This porosity correlates directly with reductions of thermal conductivity and strength, so it must be minimized during processing. Some basic properties of these fuel particle/matrix composites have been studied in the nonirradiated state [15]. As in the CVI fiber/matrix composites, the porosity produced in this work is

about 8–10%, which is on the lower end of the spectrum found in CVI processing. The SiC material manufactured through the new processing route has been tested and evaluated to assess its performance as the TCR core material.

1.2 PERFORMED WORK

Materials testing tasks were performed to build a database of mechanical and thermophysical properties for the SiC that was processed via binderjet printing and CVI. Multiple sets of specimens have been manufactured for mechanical and thermophysical tests before and after irradiation. First, a large number of mini-disk specimens (nominal 6 mm diameter and ~0.5 mm thickness) were produced for baseline and post-irradiation testing and characterization. Second, rodlet samples with three different directions were produced to measure the coefficient of thermal expansion (CTE) in those directions. Third, the 12.7 mm diameter, 1.59 mm thick disks were produced to measure elastic constants using a resonant ultrasonic spectroscopy technique. At this writing, the three main campaigns described have been performed to obtain the key mechanical and thermophysical performance data for assessment of the SiC material synthesized via binderjet printing and CVI:

- Baseline mechanical and thermophysical properties were measured from the disk specimens printed for different sizes and orientations, including equibiaxial flexural failure strength, elastic constants, thermal diffusivity and conductivity, density, and the CTE.
- A neutron irradiation experiment was performed for the 3D-printed SiC material. Six irradiation capsules containing the 3D-printed 6 mm diameter SiC disk samples were irradiated at the High Flux Isotope Reactor (HFIR) to 2.3 dpa over a temperature range of 400–850°C.
- The post-irradiation examination (PIE) of mechanical and thermophysical properties was completed, which included evaluation to obtain equibiaxial flexural failure strength data and thermal diffusivity and conductivity measurements. Electron microscopy was also performed on the irradiated and nonirradiated SiC microstructures to characterize defect morphologies, irradiation-induced degradation, and phase or crystal structure changes.

This report presents the mechanical and thermophysical property data of 3D-printed SiC before and after neutron irradiation that has been accumulated so far in the TCR program. The SiC database that has been built as part of the program will be used to assess the SiC fuel matrix material for TCR and to provide feedback to the new SiC synthesis route and core structure design. Since the majority of the baseline test data was reported in the last year's milestone report [19], this report is particularly focused on assessment of the 3D-printed SiC with irradiation-induced displacement damage. A summary of the irradiation experiment is presented herein, followed by the results and discussion on the radiation-induced changes in thermal and mechanical properties. In addition, the microstructure of the material after irradiation-induced damage is characterized.

1.3 PURPOSE OF DOCUMENT

The purpose of this document is to quantify and summarize the mechanical and thermophysical properties of SiC produced using an advanced manufacturing approach (binderjet printing plus CVI). This property dataset is intended for use by the core component manufacturers, modelers, and reactor designers in the TCR program and by other researchers. It can also be used for future reactor designs or applications for which these materials and manufacturing processes are of interest.

2. MATERIALS AND SPECIMENS

2.1 A COMBINED PROCESS OF BINDERJET PRINTING AND CVI

Binderjet 3D printing that is followed by a densification process is a unique technology performed at near room temperature, so it hardly alters the feedstock powder. CVI is a high temperature process used to turn a porous material into a more solid form by filling up pores and depositing crystals. A novel methodology that combines these processes was recently developed to produce carbide ceramics. This new methodology has been leveraged to produce an inert SiC fuel matrix or structure for the TCR core [22, 26-28]. Specimens used for this testing and characterization task were produced using the newly established manufacturing process.

The properties of the SiC materials described in this document were derived from α -SiC (hexagonal phase) feedstock powder with $\sim 20 \mu\text{m}$ diameter from Sigma Aldrich with a purity $>99.5\%$. The Innovent binderjet printing systems from ExOne Company (North Huntingdon, Pennsylvania) were used to produce the test specimens. An aqueous binder (Binder 05 from ExOne) was used during printing; this binder underwent curing at 190°C for 6 h in air. The curing step drives off the majority of the aqueous binder, and the binder is almost entirely decomposed and dissociated away from the part at a higher temperature during the next step of the process.

After the green parts are binderjet printed and cured, they are transferred to the furnace for the CVI process, where they undergo densification. A mixture of H_2 gas and methyltrichlorosilane (MTS) carrier gas is injected into the CVI furnace to decompose the gases at about $1,000^\circ\text{C}$ and deposit high purity, stoichiometric, and crystalline SiC around the 3D-printed SiC powder particles. Depending on the size of each part and the processed batch, the CVI process can take hours to days to close the open porosities. Depending on details of the CVI condition, the density of the SiC disks is typically around 90% of the theoretical density of SiC ($= 3.2 \text{ g/cm}^3$) [20].

2.2 SiC SPECIMENS AND CONFIGURATIONS

Various types of specimens have been printed using the combined binderjet and CVI processing. First, a large number of mini-disk (6 mm diameter \times 0.5 mm thickness) specimens were produced for baseline and post-irradiation tests. This specimen design was used for both the baseline testing and PIE, and the results were used to build a database of mechanical properties and thermophysical properties before and after irradiation. Second, rodlet samples with three different printing directions were produced to measure the CTE in those directions. Third, the 12.7 mm diameter, 1.59 mm thick disks were produced to measure elastic constants using a resonant ultrasonic spectroscopy technique. Figure 1 shows a simple schematic of the powder bed during binderjet printing, where successive 2D XY planes are printed and stacked in the Z direction to form the 3D bed. Disks in two directions were printed with the X and Y directions parallel to the plane of XY disks and with the Z direction parallel to the plane of Z disks. These orientation definitions are used for all specimen types used in the program, including metallic specimens, for which test results are reported separately.

Table 1 lists the types of test specimens, along with information on their orientations, build identifications, and purposes. The build identification numbers (or run dates) can be used to revisit detailed printing and CVI conditions. The rod-type specimens are built along X, Y (binder deposition) and Z (layer stacking) directions. Some specimens that are characterized as “Si-doped” contain a small volume fraction ($< 3\%$) of free Si in their microstructure. TCR targets the use of Si-free 3D-printed SiC by slightly elevating the temperature during the CVI process. Nonetheless, both 3D-printed SiC variants (with and without residual free Si) are examined in this study to provide a complete analysis.

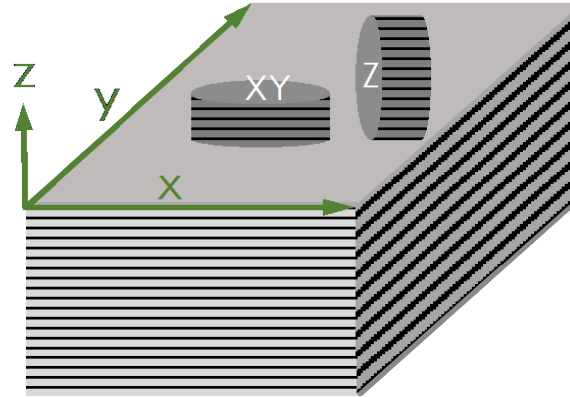


Figure 1. Schematic of orientation relationship in binderjet printing [20]: sample orientation on powder bed during binderjet printing, with the build progress indicated in the Z direction, stacking and fusing successive XY powder planes. The black horizontal lines indicate relatively low-density regions between the successively printed XY planes.

Table 1. Summary of SiC specimen builds for testing and evaluation, listing all specimens built by a combined binderjet printing and CVI process since 2019

Specimen type	Build ID run date	Sample orientation	Purpose
Mini-disk: Ø6 × 0.5 mm	LSCVI19 (Si-doped)	XY	- Equibiaxial flexural strength test - Thermal diffusivity measurement - Neutron irradiation experiment
	LSCVI29: 20191004 1-1 20191004 1-2	XY	
	LSCVI31	Z	
	LSCVI86 20201207 2-3 20201208 2-2	XY	- Equibiaxial flexural strength test
	LSCVI78 20210104 2-1 20210104 2-2 20201217 2-1 20201217 2-2	Z	
Mini-rodlet: Ø6 × 10 mm	20200316 2-1 (X) 20200317 2-3 (X) 20200316 2-2 (Y) 20200316 2-3 (Z) 20200317 2-1 (Z)	X, Y, Z	- Dilatometry for the CTE
Disk: Ø12.7 × 1.59 mm	20200331 2-3 20200401 2-2 20200401 2-3	XY	- Resonant ultrasound spectroscopy for elastic constants (for use in strength calculation)

Note: XY – layers on X-Y planes stacking in the Z-direction; X, Y, Z – sample growth directions; GL=gauge section length

In addition, a few examples of macro-scale morphologies of a 3D-printed SiC taken from optical microscopy are displayed in Figure 2. These morphologies are typically used for a quick assessment of the combined binderjet/CVI process. They show the cross section of XY disks, with the Z direction indicating the direction of the build [20]. Figure 2(a) is a low-magnification cross section view of a poorly

infiltrated XY disk, Figure 2(b) is a higher-magnification view of the same disk, and Figure 2(c) shows the cross section of an optimally infiltrated XY disk. All disks in this study conform to the infiltration conditions shown in Figure 2(c). Also, the first two images are included to illustrate that there is an anisotropy in powder density after the binderjet printing step. In essence, the powders are relatively densely packed in each of the XY planes and between each XY layer, and as the build progresses in the Z direction, the low-density regions form. This observation is important for interpretation of the data in the later sections of the manuscript. Note that when infiltration conditions are optimal, as shown in Figure 2(c), this directional variation in density is no longer readily apparent after densification. Note that both faces of the disk specimens were polished to a roughness of ~ 1 micrometer.

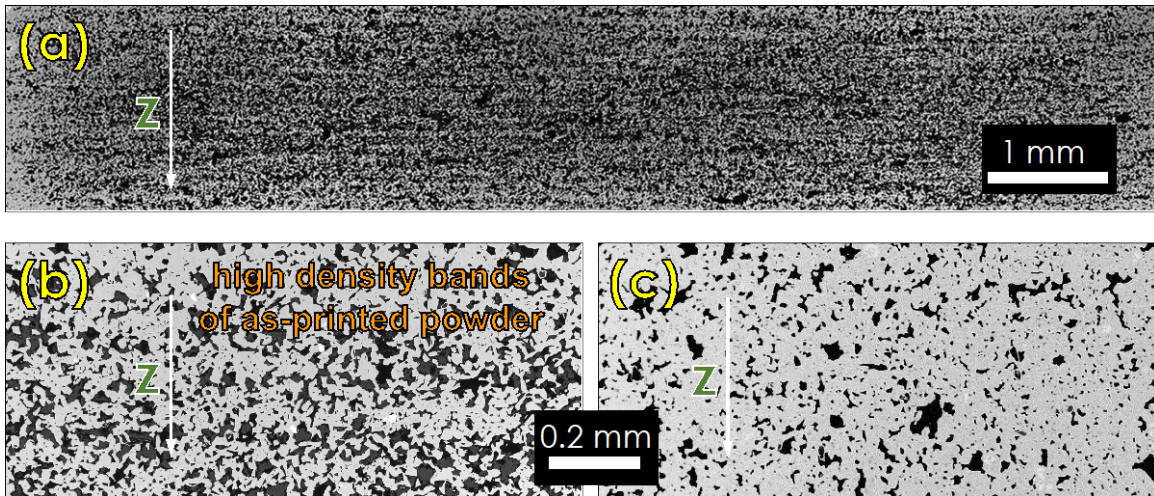


Figure 2. Porous morphology of 3D-printed SiC: (a) low magnification and (b) high magnification optical image of cross section of a poorly infiltrated XY disk, and (c) cross section of an optimally infiltrated XY disk.

3. BASELINE TESTING AND CHARACTERIZATION

This section presents mechanical and thermophysical test data obtained before irradiation. These baseline data can be compared with the corresponding data from the testing and evaluation performed after neutron irradiation at HFIR [21] and used as the input data for the calculation of property parameters. For instance, Poisson's ratio measured for 3D-printed SiC is used to calculate failure strength.

3.1 FAILURE STRENGTH OF 3D-PRINTED SiC

Mechanical testing has been performed primarily to establish the baseline mechanical properties of the additively manufactured SiC materials with different orientations. The following subsections present the equibiaxial flexural strength test method, as well as the strength test results for the SiC specimens after the combined processes of binderjet printing and CVI. In the data presentation, all datasets are analyzed with Weibull statistics [22].

3.1.1 Equibiaxial Flexural Strength Test

A miniaturized equibiaxial flexural strength test method was used to measure the fracture strengths of SiC materials with thin disk (0.5 mm thickness \times 6 mm diameter) specimens. In this procedure, a disk specimen is loaded up to fracture in a concentric ring-on-ring mode, as illustrated in Figure 3. This concentric bending mode can induce a relatively uniform biaxial tensile stress on the lower surface of the

disk specimen. Typically, specimen fracture occurs when the tensile stress at the weakest point in the lower surface layer reaches a critical level. This method is described in the American Society for Testing and Materials (ASTM) standard test method C1499-09 [23].

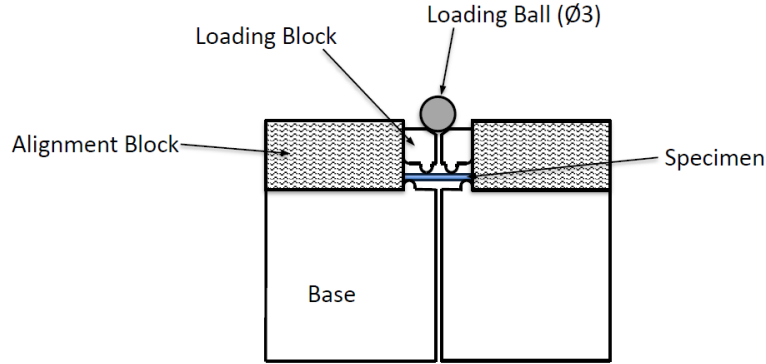


Figure 3. Schematic section view of fixturing and test specimen for equibiaxial flexural strength testing. Note that the diameters of upper and lower contact rings are 2 and 5 mm, respectively.

Two testing systems—an MTS Insight Electromechanical Testing System at the Low Activation Materials Development and Analysis (LAMDA) facility and a TestResources Servo-Electric Dual-Frame System at the Manufacturing Demonstration Facility (MDF)—were used for the biaxial flexural strength testing of the 6 mm diameter specimens. The fracture or breaking load, which is the maximum or failure load obtained in each test under monotonic loading, is converted to the fracture stress at the surface of disk specimen (σ_f). The disks were 6 mm in diameter and 0.48 mm thick, on average. The measured thicknesses of the individual specimens were used in the calculations. The formula for the equibiaxial failure strength, σ_f , of a circular plate specimen in units of MPa is given in Eq. (1) [23],

$$\sigma_f = \frac{3F}{2\pi h^2} \left[(1 - \nu) \left(\frac{D_S^2 - D_L^2}{2D^2} \right) + (1 + \nu) \ln \left(\frac{D_S}{D_L} \right) \right], \quad (1)$$

where

- F = the breaking (fracture) load [N],
- h = the specimen thickness [mm],
- D = the specimen diameter [6 mm],
- D_S = the support ring diameter [2 mm],
- D_L = the load ring diameter [5 mm], and
- ν = Poisson's ratio.

3.1.2 Statistical Treatment of Failure Strength Data

The failure strength of 3D-printed SiC for the fuel matrix, a key TCR core structural material, is of great importance to the structural integrity of the core. Because the binderjet SiC materials with or without CVI are brittle materials, their failure strength is controlled by the cracking strength of the “weakest link”; that is, fracture occurs at the critically sized and located flaw present in the sample. This type of behavior is well described by Weibull statistics [22], in which crack-initiating flaws are assumed to be randomly distributed throughout the tested volume. Because the same volume specimens are tested for each batch of specimens, the cumulative distribution function or probability of failure for the Weibull distribution is expressed by

$$P_f(\sigma_f) = 1 - e^{-\left(\frac{\sigma_f}{\sigma_0}\right)^m}, \quad (2)$$

where m is the Weibull modulus, and σ_0 is the characteristic strength or scale parameter. The two parameters in the function, m and σ_0 , are also called the shape and scale parameters, respectively. The probability of failure is calculated by

$$P_f = (i - 0.3)/(N + 0.4), \quad (3)$$

where i is the rank of failure strength in a set of N data [24]. These results may be extended to predict failure probability in larger geometries by normalizing against the volume or surface area of these tests (i.e., 1.57 mm³ and 3.14 mm²).

The two parameters in Eq. 2, m and σ_0 , can be determined by plotting the data as a log-log graph or a so-called Weibull plot using

$$\text{Ln}(-\text{Ln}(1 - P_f)) = m \times \text{Ln}(\sigma_f) - m \times \text{Ln}(\sigma_0). \quad (4)$$

On this log-log scale, the data points will follow a linear trend if the failure strength data follow a Weibull distribution or if they are dependent on only one failure mechanism. The least squares fit of the line described by Eq. (4) yields estimates for the shape and scale parameters of the Weibull distribution.

3.1.3 Baseline Failure Strength Data for 3D-Printed SiC

The datasets of failure stress calculated using Eq. (1) were statistically treated using the Weibull statistics model [22] described above. The probability of failure (P_f) data for the 3D-printed SiC with CVI were calculated using Eq. (3). Figure 4 compares the Weibull plots for the 3D-printed SiC and CVD SiC, which shows that all datasets fit reasonably well to their respective regression lines. The Weibull parameters determined by the regression lines are summarized in Table 2. The Weibull moduli measured are within the range of 7 to 14, which is a typical range for SiC materials [8, 25, 26], and no evidence of a clear difference between the binderjet/CVI processed SiC and the reference CVD SiC was found. The results indicate that the characteristic strength of the three 3D-printed SiC variants is approximately 20% lower than the CVD SiC. Similarly, the mean characteristic strength of the 3D-printed SiC is 22–27% lower than that of the CVD material (~390 MPa). Overall, similar failure probability behaviors were observed for the three 3D-printed SiC variants, although the data for the 3D-printed SiC with XY orientation show a slightly higher probability of failure in the low failure strength region (< ~310 MPa). Comparison of these failure strength data also indicates that neither the effect of specimen orientation (XY versus Z) nor the effect of Si doping (in 3D-XY-Si) significantly affects the probability of failure and strength behavior in the 3D-printed materials. This comparison also shows that the probability of failure curve for the CVD SiC extends to the strength region of the 3D-printed SiC samples (< 300 MPa), although its overall strength is clearly higher than its printed SiC counterparts.

Although the multiple types of flaw distributions or simultaneous occurrences of volume and surface defects can initiate cracks, the role of flaws and pores in the surface layer should be dominant in the failure of these SiC disks under the present equibiaxial bend loading. The relatively monotonically linear shapes of the Weibull plots indicate that the cracking mechanism, most likely initiating from the specimen's lower surface where the maximum tension stress occurs, does not change in each set of specimens. Finally, it should be also noted that the flexural failure strength is dependent on Poisson's ratio (ν) of the test specimen, as indicated in Eq. (1). A newly measured Poisson's ratio (0.124) was used for the 3D-printed SiC specimens (see details in Section 3.2.6), and a higher value (0.21) was used for the

CVD SiC. Therefore, the lower failure strengths measured from the 3D-printed SiC materials are partially due to the lower Poisson's ratio.

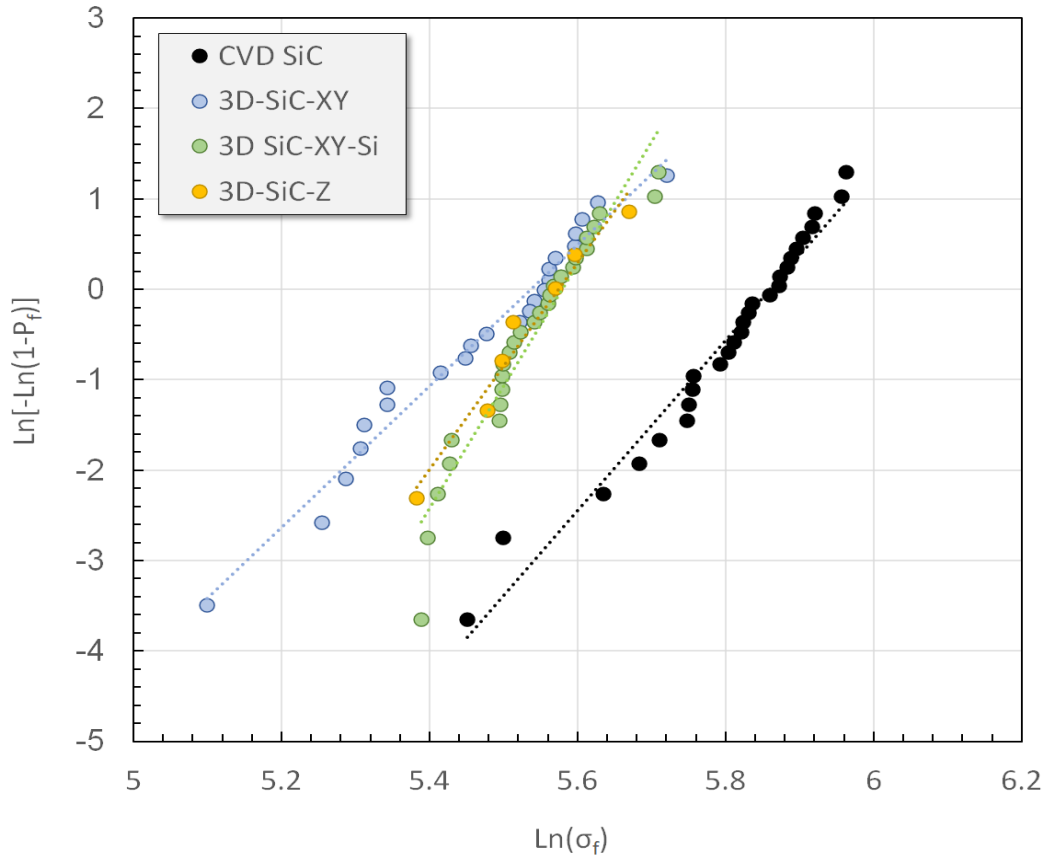


Figure 4. Weibull plots of SiC failure strength data from equibiaxial flexural strength testing.

Table 2. Summary result of Weibull statistics analysis for equibiaxial flexural strength tests

Materials	Specimen ID	Dimension (mm)	Weibull modulus (=m)	Scale parameter (=σ ₀) (MPa)	Mean failure strength (MPa)
CVD SiC	C0i (i=1-27)	Ø6 × 0.49	9.4	404	390
3D-SiC-XY	XYi (i=1-23)	Ø6 × 0.48	7.8	319	286
3D SiC-XY-Si	XSi (i=1-27)	Ø6 × 0.47	13.6	333	303
3D-SiC-Z	Zi (i=1-7)	Ø6 × 0.49	11.4	331	305

3.1.4 Cause of Variation in Failure Strength of SiC

The failure strength of ceramics like SiC is known to be dependent on dimensional and microstructural conditions. For example, the size of the specimen affects the measured strength of SiC since its failure is statistically controlled by the number of critical defects contained in the sample that is proportional to the volume or surface area [25, 26]; the processing route and condition significantly influence the failure strength of SiC, because those factors determine the type, size, and density of the defects critical to failure initiation. A series of flexural strength tests were planned to elucidate the effects of these dimensional and structural variables on the failure behavior of 3D-printed SiC materials. The data presented below are from the first batch of the disk specimens printed for two different thicknesses and orientations.

Figure 5 compares two sets of Weibull plots for the 3D-printed SiC specimens with different sizes and orientations: ~ 0.5 mm/Z-orientation and ~ 0.7 mm/XY-orientation. Note that these 0.7 mm thick disk specimens are slightly thicker than the ASTM [23] recommended thickness of 0.08–0.5 mm for the current jig dimensions and the 6 mm diameter specimen. The mean failure strengths and Weibull parameters from these datasets are summarized in Table 3. Four sets of data were produced for the thinner specimens, and the variation among these specimen sets might represent the variation in location (and thus temperature) within the CVI furnace. The surfaces of these thinner specimens were polished before testing to compare the strength data in the same surface condition. The thicker specimens were not polished, so their rough surfaces led to premature crack initiation and lower strength measurements. There was a stark difference in the failure strengths of two thicknesses: the mean failure strengths of the 0.5 mm specimens were in the range of 186–265 MPa, which is more than twice the strengths of the 0.7 mm specimens, which were 87 and 96 MPa for the two sets. This difference might have been caused by the different thicknesses and surface conditions. Since the strength difference between the Z and XY specimens was not significant (based on the data in Table 2), the effect of specimen orientation in these datasets was not considered a major cause of the different strengths. However, the Weibull moduli measured are observed to be within a narrow range of 5.5 to 8.7, regardless of thickness, indicating that the specimen thickness and surface condition has little effect on the Weibull modulus. Since the Weibull modulus usually represents failure mode [25], these results indicate that there was no change in the failure mode: cracking initiated from a surface defect near the opposite side of the contact with the upper ring (Fig. 3). Ongoing studies will clarify the roles of individual variables in the failure strength.

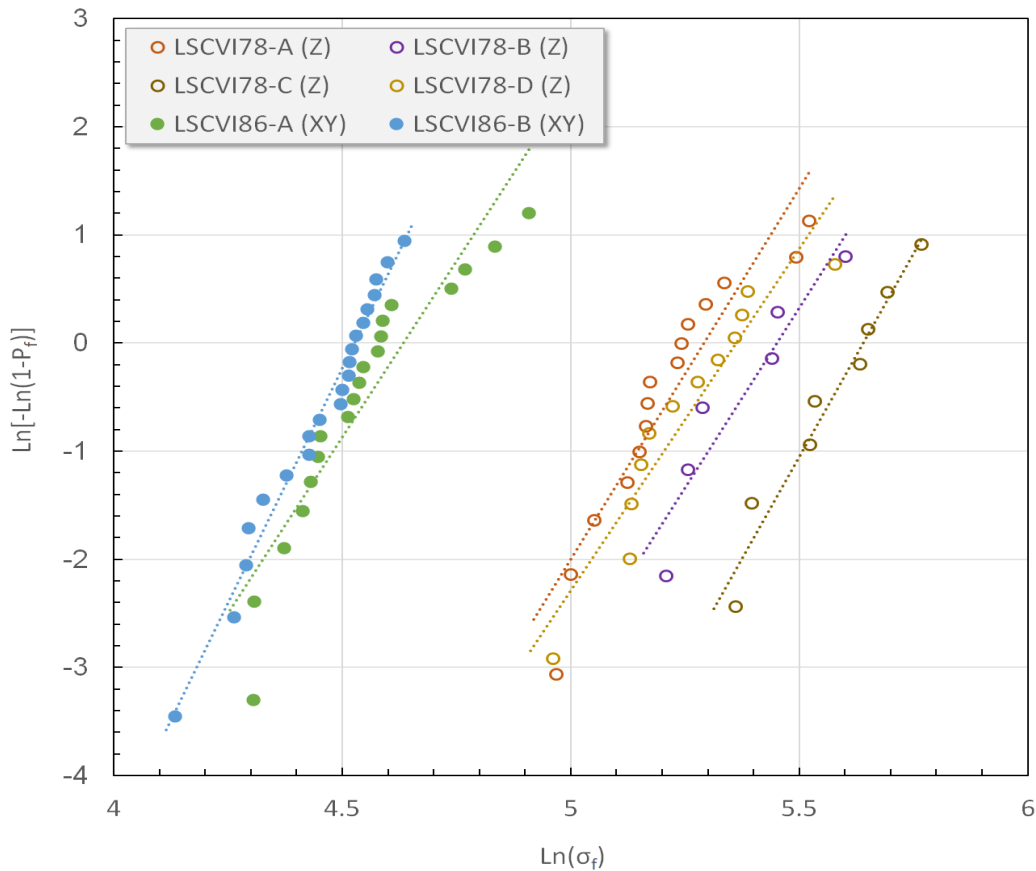


Figure 5. Weibull plots of SiC failure strength data from equibiaxial flexural strength testing with two different thicknesses and surface conditions.

Table 3. Summary result of Weibull statistics analysis for equibiaxial flexural strength tests

Materials	Specimen set I.D. (# of Tests)	Dimension (mm)	Weibull modulus (=m)	Scale parameter (=σ ₀) (MPa)	Mean failure strength (MPa)
3D-SiC-Z	LSCVI78-A (15)	Ø6 × 0.47	6.9	199	186
3D-SiC-Z	LSCVI78-B (6)	Ø6 × 0.48	6.7	233	218
3D-SiC-Z	LSCVI78-C (8)	Ø6 × 0.47	7.5	281	265
3D-SiC-Z	LSCVI78-D (13)	Ø6 × 0.48	5.5	218	202
3D-SiC-XY	LSCVI86-A (19)	Ø6 × 0.72	6.5	103	96
3D-SiC-XY	LSCVI86-B (21)	Ø6 × 0.72	8.7	93	87

3.2 THERMOPHYSICAL PROPERTIES OF 3D-PRINTED SiC

A series of measurements was carried out using various equipment at the ORNL Materials Science and Technology Division to obtain data on the thermophysical properties of 3D-printed SiC. The resulting database can be used in core design and for baseline property data for comparison with post-irradiation test results. Samples were prepared to measure (1) thermal diffusivity, (2) density, (3) the CTE, specific heat (C_p), and elastic constants. Figure 6 shows the three main pieces of equipment used to take these measurements. The following sections describe the experimental details and results.



Figure 6. Laser flash system for thermal diffusivity (left), differential scanning calorimeter (DSC) for specific heat (C_p) (center), and CTE (right) testing systems

3.2.1 Thermal Diffusivity

The thermal diffusivity of 6 mm diameter × 0.5 mm thick SiC disks was measured using the Netzsch LFA457 Microflash system, shown in on the left in Fig. 6. The test follows ASTM E1461-07 [27] and used a Nd:glass laser ($\lambda = 1.06 \mu\text{m}$) to deposit a heat pulse (600 μs) on the back surface of a sample. An infrared detector (InSb: $\lambda = 3\text{--}5 \mu\text{m}$) was used to record the top surface temperature transient through a sapphire window. The half-rise time ($t_{1/2}$) was determined by software, and thermal diffusivity (α) was calculated using Parker's equation [28], assuming no heat loss:

$$\alpha = 0.139d^2/t_{1/2}, \quad (5)$$

where d is the specimen thickness. In practice, a heat loss correction using the Cowan method [29] or Clark & Taylor [30] analysis is applied, along with pulse-width correction. The diffusivity tests were performed under argon purge gas from ambient (23°C) temperature to 900°C in 100°C incremental steps. Three measurements were taken at each set temperature.

Plots of thermal diffusivity vs. temperature are shown in Fig. 7. The Z series has the highest room temperature value of 25 mm²/s, the XY samples have a value of 15 mm²/s, and the Si-doped XS samples (printed on X-Y plane) have the lowest value of 10 mm²/s. As a reference, the thermal diffusivities of SiC at room temperature for fully dense 3C, 4H and 6H SiC are 160, 170 and 220 mm²/s, respectively [31]. The microstructural features in the sintered SiC materials—specifically grain boundaries and defects—play important roles in scattering phonons, so their thermal diffusivities at room temperatures are in the range of 50–80 mm²/s. This is typically lower than the thermal diffusivities of fully dense SiC materials. However, the porosity of the 3D-printed SiC materials results in relatively lower thermal diffusivity. Even after the CVI process, the pores are not completely filled with SiC, so the microstructures of these materials still have more defects to scatter phonons. As seen in Figures 1 and 2, both the dense and less-dense layers in the Z specimens are aligned parallel with the heat transfer direction. These specimens have more continuity and less reflectivity in the heat transferring direction, so the thermal diffusivity of the Z specimens is relatively higher than that of the XY specimens.

Of the 3D-printed materials, the microstructural differences in the different series result in anisotropy in heat conduction. Thermal diffusivity (α) values of all three series decrease with increasing temperature, which is typical for lattice thermal conduction of ceramics (Umklapp scattering). The differences in the three principal directions are consistent with the 3D printing build directions and the resulting microstructures. During cooling, measurements were taken at 300 and 100°C for all specimens. There were no observable changes in the measurements, which indicates that all three SiC materials were stable after heating to 900°C.

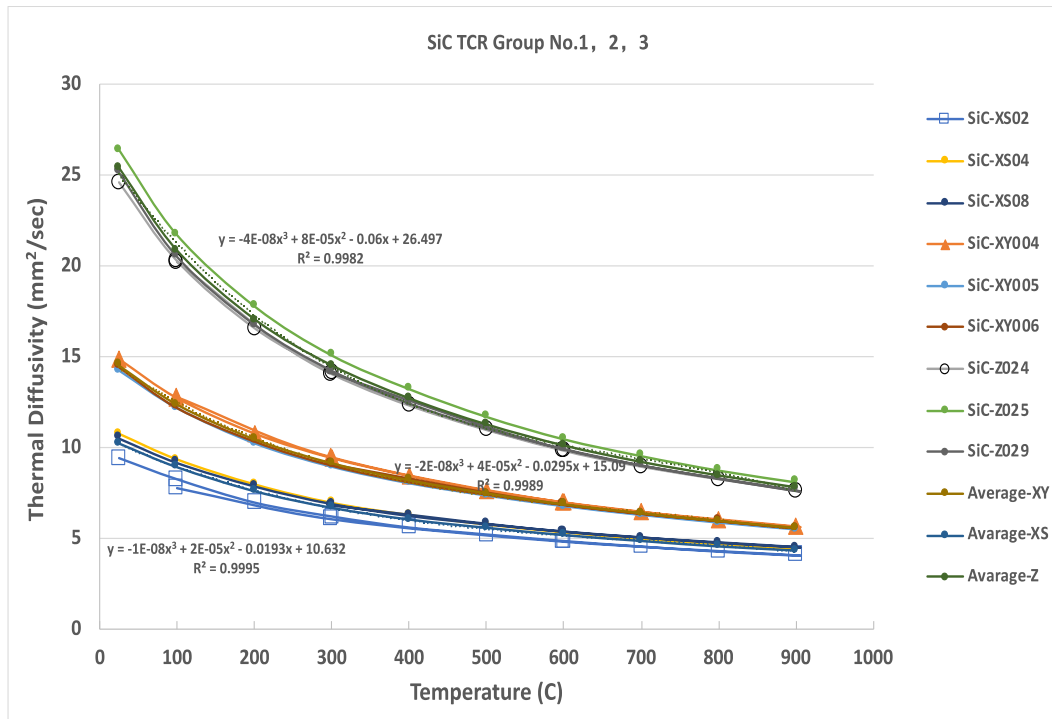


Figure 7. Thermal diffusivity of 3D-printed SiC after CVI.

Thermal diffusivity data of the three series were averaged using the three duplicates and shown as averages for each series. A simple third-order polynomial curve fit was used:

$$\alpha = A + BT + CT^2 + DT^3, \quad (6)$$

where T is temperature in °C. Curve fit parameters are shown in Table 4. They are empirical equations for values with a range of 23–900°C.

Table 4. Curve fitting parameters in the thermal diffusivity equation for the XS, XY, and Z series specimens

Series ID	A	B	C	D
XS	10.632	-0.0193	2.369E-5	-1.120E-8
XY	15.090	-0.0295	3.705E-05	-1.792E-08
Z	26.497	-0.0600	7.676E-05	-3.724E-08

3.2.2 Density Evaluation

The density (ρ) of the SiC specimens was measured using the mass and volume of the thermal diffusivity samples. Because the measured dimensions of the miniature disk samples are thought to include errors, the density data presented are not highly accurate, although they can clearly show the difference from processing routes. As shown in Fig. 8, nine 3D-printed specimens showed some scatter ranging from 2.75 to 2.94 g/cm³, which is 85.7 to 91.6% of the theoretical density of 3.21 g/cm³. The average value was 2.86 g/cm³ (89% dense). The scatter was also a result of the small size of the specimens (6 mm diameter, 0.5 mm thick). In addition to the errors originating from the small dimensions, there were also some errors caused by the laser-engraved identification letters, which might have caused a slight overestimation of the volume and thus lowered the density. For comparison, three CVD SiC specimens with the same dimensions were also measured, for which the average density was 3.17 g/cm³, or about 98.8% of ideal density. For use in later thermal conductivity calculations, the measurements of three samples in each specimen group were averaged $\rho_{xs} = 2.792$ g/cm³, $\rho_{xy} = 2.860$ g/cm³, and $\rho_z = 2.919$ g/cm³.

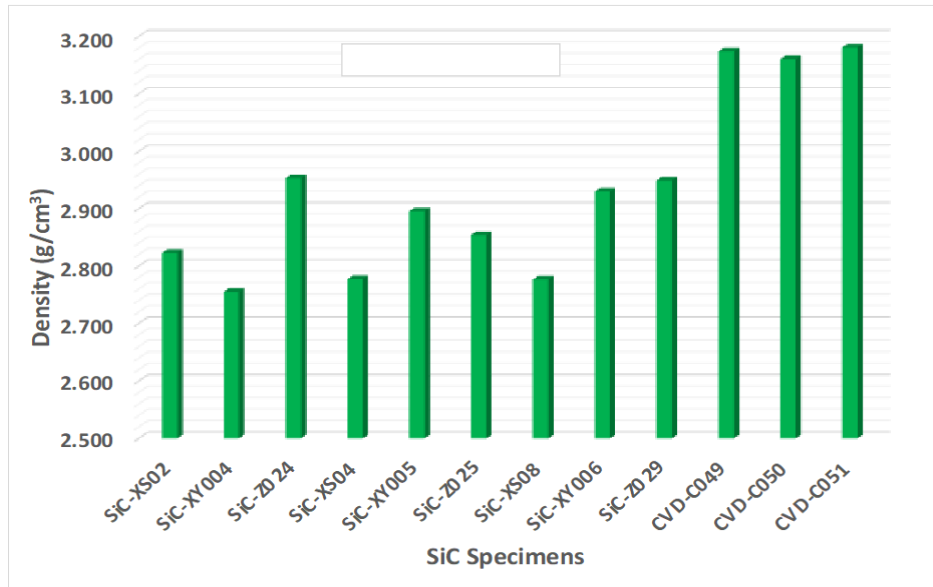


Figure 8. Density of 3D-printed SiC after CVI and CVD SiC.

3.2.3 Specific Heat Capacity

Specific heat capacity of the 3D-printed SiC was measured using a Netzsch Pegasus 404C, a differential scanning calorimeter (DSC) following guidelines specified in ASTM E1269 [32], over the temperature span from room temperature to 900°C at a 10°C/min heat/cooling rate. The ratio method includes a baseline run (two empty Pt pan/lid sets), a reference run with a sapphire standard, and a sample run. The specific heat of the sample, C_p , is calculated as follows:

$$C_p = \frac{DSC (sample-baseline)}{m_{sample} * HR * Sensitivity}, \quad (7)$$

in which the DSC signal is in μV , and HR is the heating rate. The sensitivity of the DSC is

$$Sensitivity = \frac{DSC (sapphire-baseline)}{m_{sapphire} * HR * C_p(sapphire)}. \quad (8)$$

If the ratio between the specific heat capacities of the sample and reference sapphire is used, then the sample C_p becomes independent of HR and sensitivity:

$$C_p = \frac{DSC (sample-baseline) * m_{sapphire}}{DSC (sapphire-baseline) * m_{sample}} C_p(sapphire). \quad (9)$$

Figure 9 shows the calculated C_p values of three SiC samples during heating and cooling. The scatter could be caused by sample-to-sample variations, baseline shifting, and radiation effects between the sapphire standard and the SiC sample. The values for heating and one set of cooling curves are consistent with the literature [33]. The cooling data showed lower values, especially at high temperatures. A physics-based model was not used for curve fitting because of the lack of lower temperature ($< 0^\circ C$) data. The heating and cooling C_p curves are represented by third-order polynomials. Three curve-fitting results are plotted in Fig. 10, along with the handbook values for CVD SiC [8]. The differences in the three directions were not as clear as the differences for thermal diffusivity. Since C_p is more sensitive to composition than microstructure, the scatter is likely due to variations in sample and experimental uncertainties.

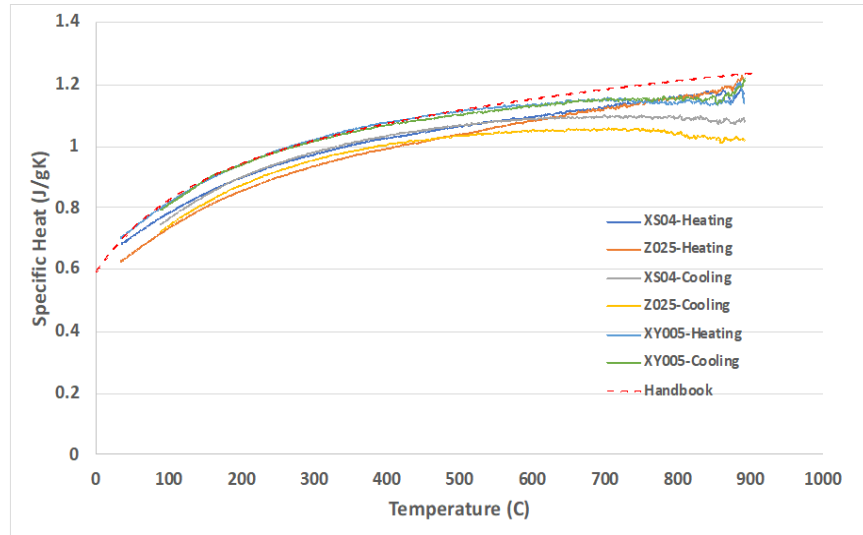


Figure 9. C_p vs. temperature plots of three 3D-printed SiC samples during heating and cooling (SiC Handbook values are represented by the dashed red line).

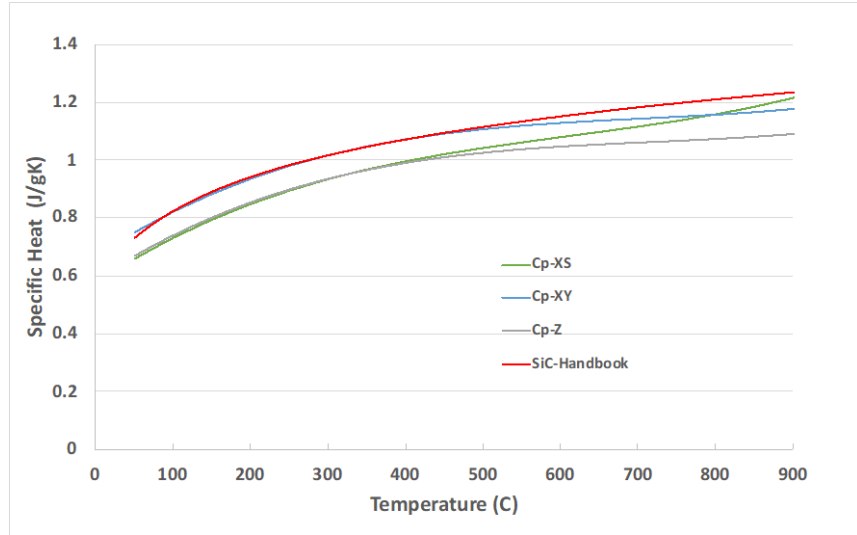


Figure 10. C_p (curve-fitting of heating data) in three printing directions compared with the reference data (Eq. (10) in the SiC Handbook [8]).

3.2.4 Thermal Conductivity

The thermal conductivity of each of material was calculated using Eq. (10) from the thermal diffusivity (α), density (ρ), and specific heat (C_p) data, which were measured and evaluated as described in the previous sections.

$$k = \alpha \rho C_p, \quad (10)$$

In the calculation of thermal conductivity, the average values of thermal diffusivity measurements (Fig. 7) were used, as were the average measured densities for each direction, and the curve fit for C_p in Fig. 10 was applied in Eq. (10). The thermal conductivities of the three SiC groups are displayed in Figure 11.

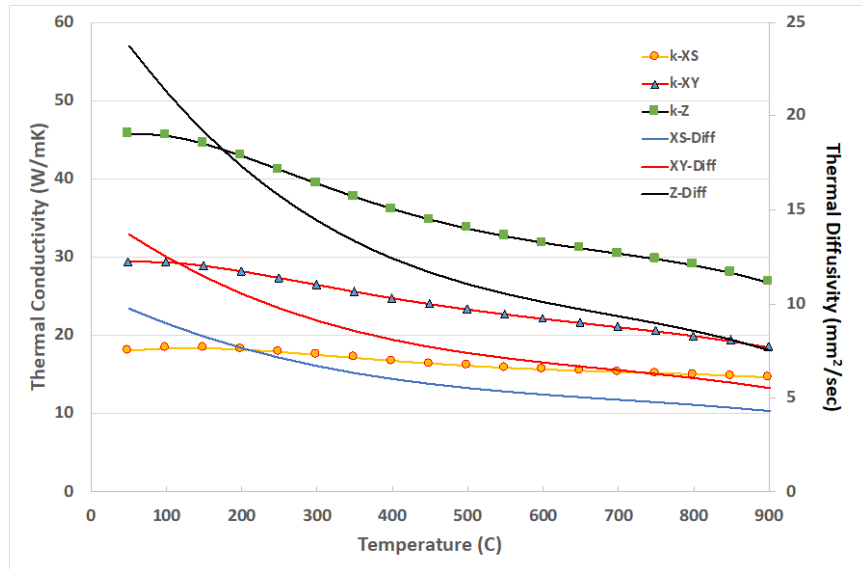


Figure 11. Thermal diffusivity and calculated thermal conductivity of three 3D-printed SiC samples with different orientation.

The calculated thermal conductivity showed a slower decline with increasing temperature when compared with the temperature dependence of thermal diffusivity (see the solid lines without data markings). This may be mainly because (1) the specific heat (C_p) has a general trend of increasing with temperature over the same temperature range, and (2) the 3D-printed materials have relatively lower thermal diffusivities in the low temperature region (typically 40–50% of the CVD SiC thermal diffusivities), which results in a lower temperature dependence.

3.2.5 Coefficient of Thermal Expansion

A Theta Dilatronic IX dual-push-rod differential dilatometer was used to measure the coefficient of thermal expansion (CTE) of nine specimens—three samples each per orientation. The samples were 10 mm in length and 6 mm in diameter. A National Institute of Standards Technology (NIST) standard reference material (SRM) sapphire rod 10 mm in length was used for comparison. The system was maintained at a constant temperature of 30°C as controlled by a water bath set at the reference temperature. Both the heating and cooling rates were set at 3°C/min. The alumina tube containing the specimen was evacuated three times and back filled with ultra-high purity (UHP) helium. The helium purge gas also passed through an oxygen gettering furnace (CENTOR), and a flow rate of 5 mL/min was maintained throughout the measurements.

Figure 12 shows the mean CTE vs. temperature plots for all nine specimens. The CTE values increased from $2.5 \times 10^{-6} \text{ K}^{-1}$ at 70°C to about $4.7 \times 10^{-6} \text{ K}^{-1}$ at 900°C, with little variations among specimens. The noise at low temperatures was due to the furnace’s slow reaction to follow the programmed heating rate. As shown in Figure 12, after 100°C, the CTE values became more stable. The measurements show that the temperature dependencies in all nine samples were similar, and the CTE did not show any notable change with respect to the printing orientation or Si doping. The average CTE of the nine samples is also plotted as a function of temperature (T) in a logarithmic curve form:

$$\text{CTE} = 0.9595 \ln(T) - 1.7681. \quad (11)$$

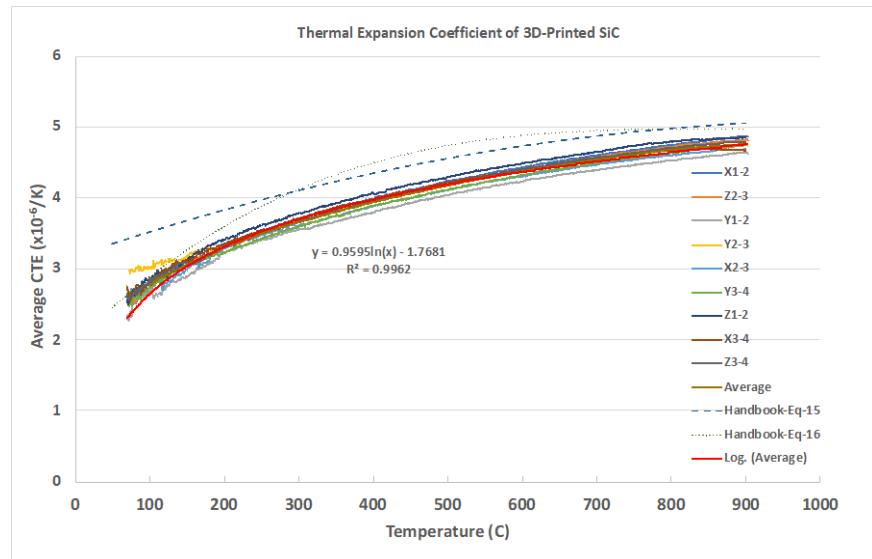


Figure 12. Coefficient of thermal expansion (CTE) vs. temperature for nine 3D-printed SiC samples. A mean value curve equation is also given, along with Eqs. (15) and (16) from the SiC Handbook [8].

The curves show CTE vs. temperature from Eq. (15: 3C-SiC in the range of 277–1,000°C) and (16: CVD 3C-SiC in the range of -148–1,000°C) from the SiC Handbook [8]). These curves are also plotted in Fig.

12, showing significant differences between the two types of 3C-SiC. The CTE results of SiC in this study exhibit lower values, and they also show that thermal expansion of the 3D-printed material is independent of the printing orientation. The corresponding volume change upon heating for the TCR design and application can be considered constant in all directions.

3.2.6 Elastic Constants and Density Measured by Resonant Ultrasound Spectroscopy

The resonant ultrasound spectroscopy (RUS) [34, 35] is used to measure the fundamental physical and mechanical properties of solid materials, such as elasticity properties. In this technique, the natural frequencies of the test materials (at which the testing objects vibrate in resonance with a mechanical excitation, typically induced by a piezoelectric transducer) are measured, and the results are used to calculate elastic constants. In general, the natural frequency depends on the elasticity, size, and shape of the specimen and its resonance with the excitation of the piezoelectric transducer. This enables determination of the elastic tensor of the testing material. A small parallelepiped-shaped sample ($\text{Ø}12.7 \times 1.59$ mm disk for this measurement) is lightly held between two piezoelectric transducers, one of which generates an elastic wave of constant amplitude and varying frequency, and the other detects the sample's resonance to record a sequence of resonance peaks. The positions of these peaks occur at the natural frequencies from which the elastic constants are determined (Fig. 13). In the measurement procedure, the vibrational response of the sample was measured at one point with a laser Doppler vibrometer (Polytec OFV-301) focused on a small strip of reflecting tape. The source transducer was driven by a function generator (National Instrument PXI-5406) transmitting a 4V peak-to-peak signal to a voltage amplifier (TEGAM 2350). The RUS experiment was repeated three times per specimen, and data were obtained for 3 specimens, resulting in 9 data points for each elastic constant. The source transducer was digitally swept up with a sequence of harmonic voltage signals progressing up to 400 kHz in frequency steps of 10 Hz.

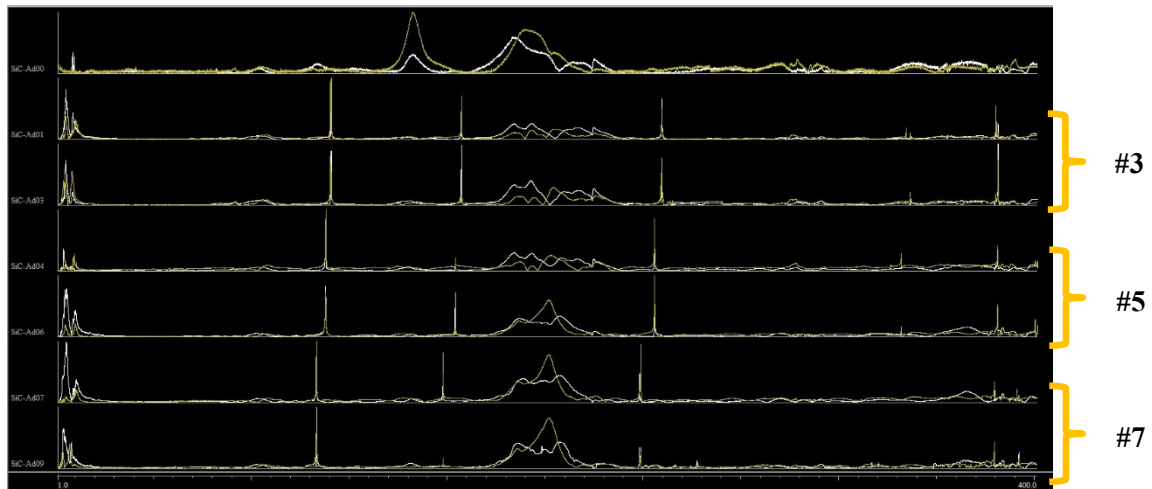


Figure 13. Examples of RUS spectra from the samples 20200331-2-3 #3 (2nd and 3rd spectra), #5 (4th and 5th spectra), #7 (bottom two spectra). Peak locations are used to calculate elastic constants.

The results of the RUS experiment for the 3D-printed SiC disks with XY orientations, Young's modulus, Poisson ratio, and density are displayed in Fig. 14. The solid blue lines are ideal values or reference measured data for CVD SiC. Overall, all three properties show relatively uniform measurements within their respective datasets, but they are significantly reduced from the theoretical or reference values. Figure 14(a) shows that the average of Young's modulus is about 246 GPa, which is significantly lower than the reference value of > 400 GPa. A similar pattern is also observed in Poisson's ratio, which is about 0.124 (note that this value for CVD SiC is about 0.21). These values were used for the failure strength

calculations, whereas the density measurements scatter about 2.6 g/cm³, which is slightly lower than the measurement based on dimension and mass (~2.9 g/cm³).

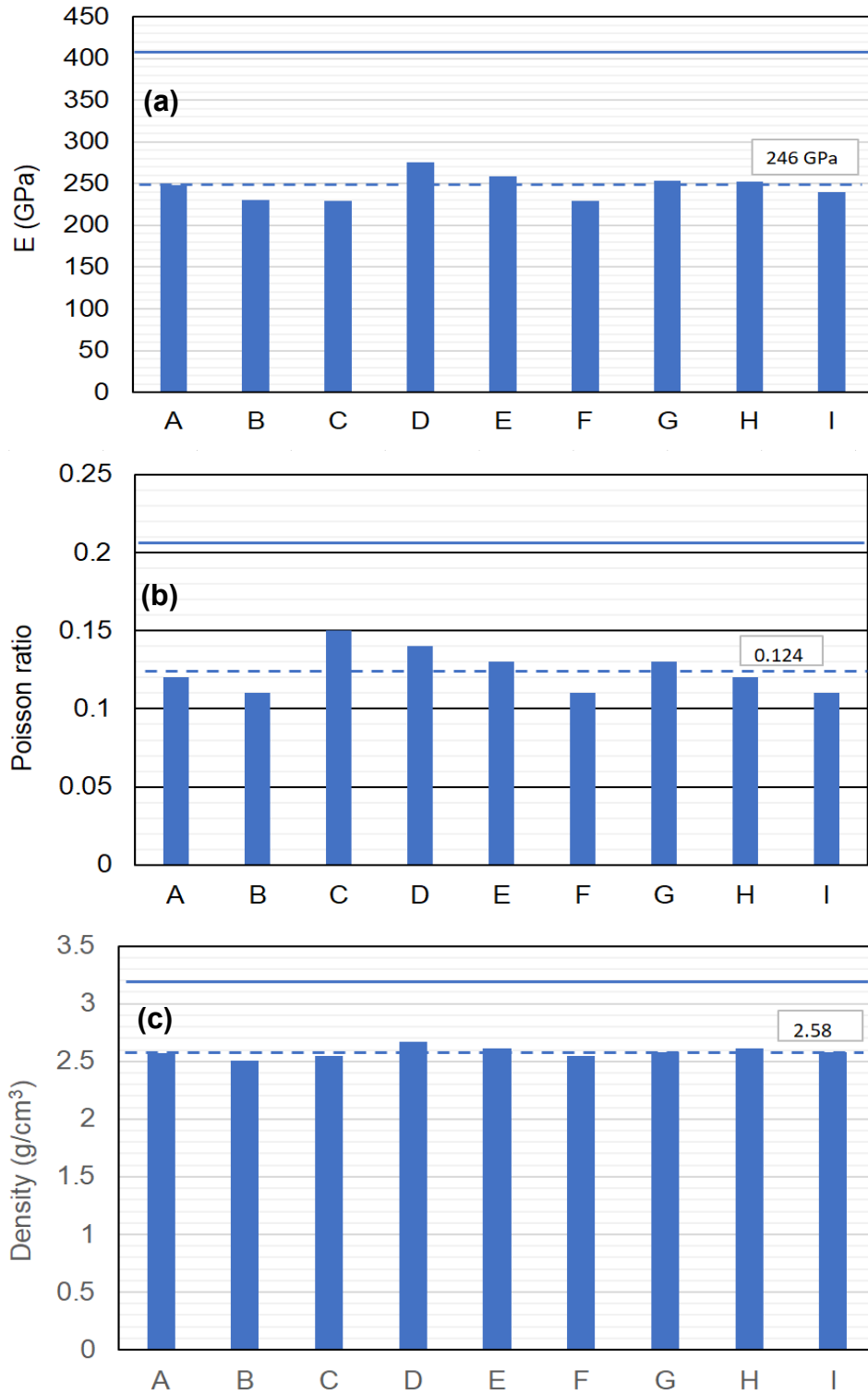


Figure 14. Elastic constants and density of 3D-printed SiC with XY orientation: (a) Young’s modulus, (b) Poisson’s ratio, and (c) density. Measurements were made using the RUS technique. Solid blue lines are ideal values or reference data for SiC.

4. NEUTRON IRRADIATION

4.1 IRRADIATION PLAN AND CAPSULE DESIGN

Neutron irradiation using rabbit capsules was planned to obtain a target displacement damage of 2 dpa at three different temperatures (400, 650, and 900°C). Each capsule contained a total of 32 SiC disk specimens, consisting of 24 binderjet/CVI SiC disks and 8 CVD SiC disks, as shown in Table 5. Each of the first three capsules contained 24 3D-printed disk specimens ($\text{Ø}6 \times 0.5$ mm) with XY orientation only, along with 8 CVD SiC disks. The second three capsules contained the same numbers of disks with Z orientation and CVD disks. Therefore, a total of 192 disk specimens, as listed in Table 6, were irradiated and tested at room temperature in the equibiaxial flexural loading condition to obtain failure strength data after irradiation. Prior to irradiation, the SiC disk specimens were ground on both sides to achieve good flatness and were subsequently laser engraved with unique specimen IDs and inserted into irradiation capsules for neutron irradiation in HFIR.

Table 5. Loading of SiC disk specimens in irradiation experiment.

Capsule ID	Target irradiation temperature (°C)	Number of 3D print + CVI disks (orientation)	Number of CVD disks
SDTR01	400	24 (XY)	8
SDTR02	650	24 (XY)	8
SDTR03	900	24 (XY)	8
SDTR04	400	24 (Z)	8
SDTR05	650	24 (Z)	8
SDTR06	900	24 (Z)	8

Figure 15 illustrates the overall irradiation capsule design. The outer container is an aluminum housing which is directly cooled on the outer surface by HFIR's primary coolant. Each capsule accommodates two stacked layers of eight specimens each on each side of a center retainer spring, for a total of 32 SiC disk specimens per capsule. SiC temperature monitors (TMs) are placed at the top and bottom of each row of specimens; eight TM plates are assembled in each capsule. The TMs are evaluated using post-irradiation dilatometry to confirm the irradiation temperature [36]. SiC retainer specimens keep the internal contents of the experiment pressed against the inner walls of the specimen holder. The holder is made of vanadium or niobium alloys, depending on the irradiation target temperature. Insulator disks are placed at the top and bottom of the assembly to reduce axial heat loss. The temperature of the capsule is controlled by varying the concentration of a helium/argon gas mixture and the size of the gas gap between the holder and the housing. Note that, because of some imperfect controls of these gas gaps and surface uniformity, the actual irradiation temperature achieved will differ from the target irradiation temperatures. Centering thimbles are placed onto the ends of the specimen holder to keep it centered within the rabbit capsule, ensuring a constant gas gap around the perimeter of the specimen holder.

Six irradiation capsules were assembled for insertion in HFIR. Figure 16 shows the parts layout for one capsule before assembly. The six capsules were irradiated in the HFIR flux trap for one fuel cycle. The irradiation dose was calculated based on the exact capsule location within HFIR using the SPECTER code [37]. Irradiation temperatures of 400, 650, and 900°C were targeted, with two capsules being tested at each temperature.

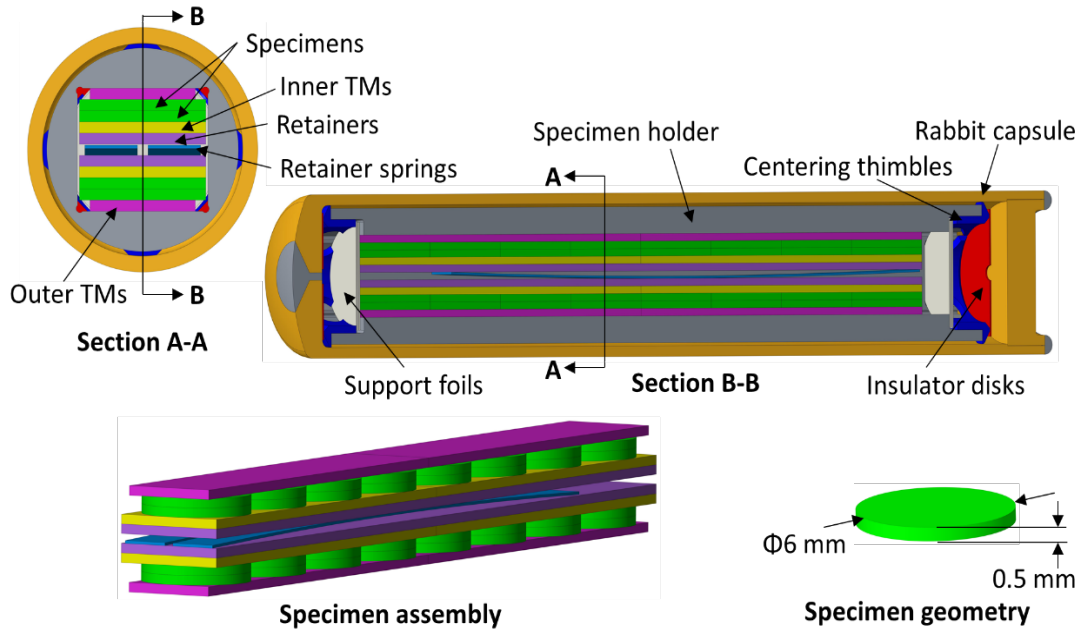


Figure 15. Rabbit capsule design for irradiation of SiC disk specimens.

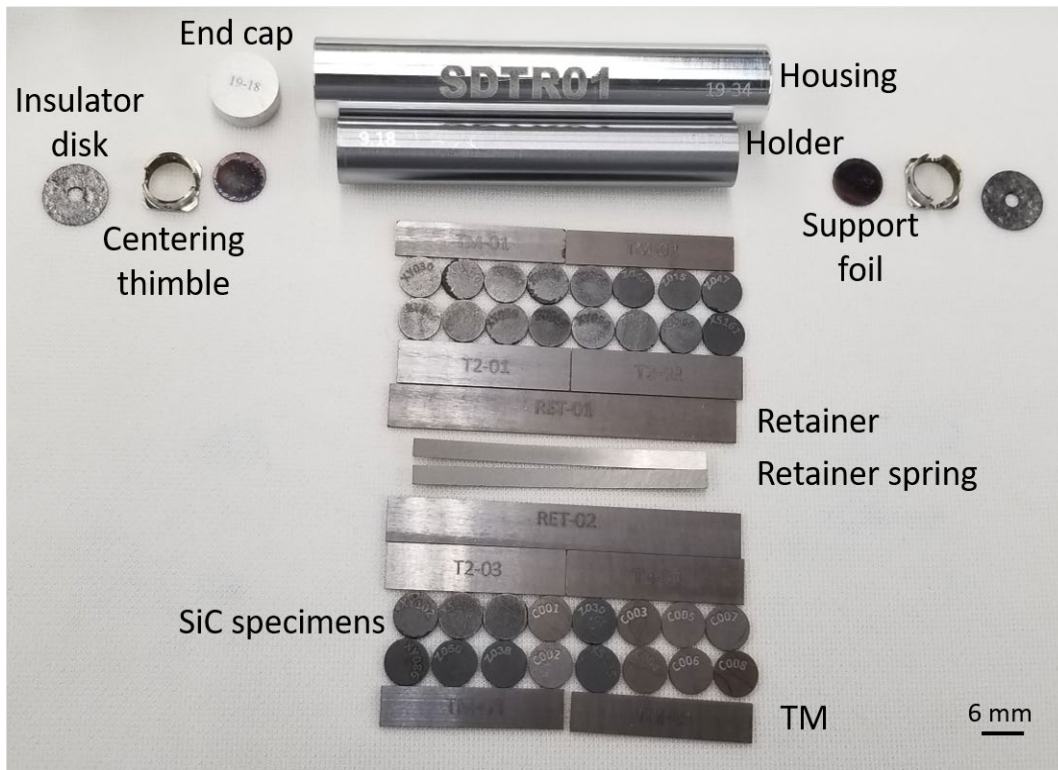


Figure 16. Parts layout for the capsule SDTR01 showing 32 SiC disk specimens, 8 temperature monitors, and other capsule structural and support components.

4.2 POST-IRRADIATION TREATMENT

After irradiation for approximately one fuel cycle, the six capsules were moved to the Irradiation Materials Examination and Testing (IMET) hot cell facility at ORNL for disassembly. All capsule components were successfully recovered, and disk samples were identified using a video camera with magnification capability. Figure 17 shows a set of SiC disk specimens recovered from a capsule after disassembly. SiC disk specimens, as well as passive SiC TMs, were shipped to the LAMDA laboratory for various characterizations and further sample preparation for microscopy.

The TMs were analyzed via dilatometry measurements to confirm the irradiation temperatures [36]. The irradiation temperatures from ANSYS finite element software, which were based on the assembled dimensions of capsule internals and core locations of rabbit capsules, are listed in Table 6, along with experimental TM measurements. This table shows the entire irradiation test matrix. The actual temperatures were determined from experimental analysis of TM coupons after irradiation, and the actual displacement damage dose was 2.3 dpa. The actual temperatures were within 2–9% of the design target temperatures. Although it was determined that these measured irradiation temperatures did not match the target irradiation temperatures precisely in planning (i.e., 400, 650, and 900°C), the temperatures still comply well with the original intention of the experiment, which was to test SiC materials at representative low, middle, and high irradiation temperatures in order to cover the possible operation temperature range of the TCR fuel matrix.

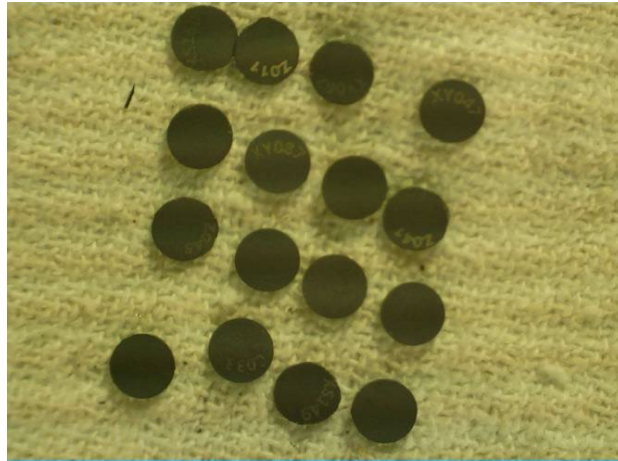


Figure 17. Disk specimens recovered after hot cell disassembly of capsule SDTR05 (showing 16 of the 32 disks from the capsule)

Table 6. Irradiation test matrix for SiC disk specimens determined after irradiation.

Capsule ID	dose (dpa)	Design target temperature (°C)	Actual temperature from TM analysis (°C)	TM uncertainty (±°C)
SDTR01	2.3	395	406	11
SDTR02	2.3	650	628	27
SDTR03	2.3	896	879	71
SDTR04	2.3	401	364	9
SDTR05	2.3	658	617	25
SDTR06	2.3	916	849	26

5. POST-IRRADIATION EXAMINATION AND PROPERTIES

5.1 FAILURE STRENGTH AND STATISTICAL BEHAVIOR

Monotonic equibiaxial ring-on-ring mechanical tests were performed to assess the failure strength of the 3D-printed SiC disks before and after irradiation. All failure strength tests for the 6 mm diameter disks in the XY and Z orientations were performed at room temperature in conformance with ASTM C1499 [23] (see Section 3.1.1 above). The strength data of 3D-printed SiC disks as determined from equiaxial ring-on-ring tests is shown in Fig. 18 as Weibull distributions. The detailed results are also captured in Table 7, which shows the failure strength values determined for XY and Z disks before and after irradiation at various temperatures to 2.3 dpa.

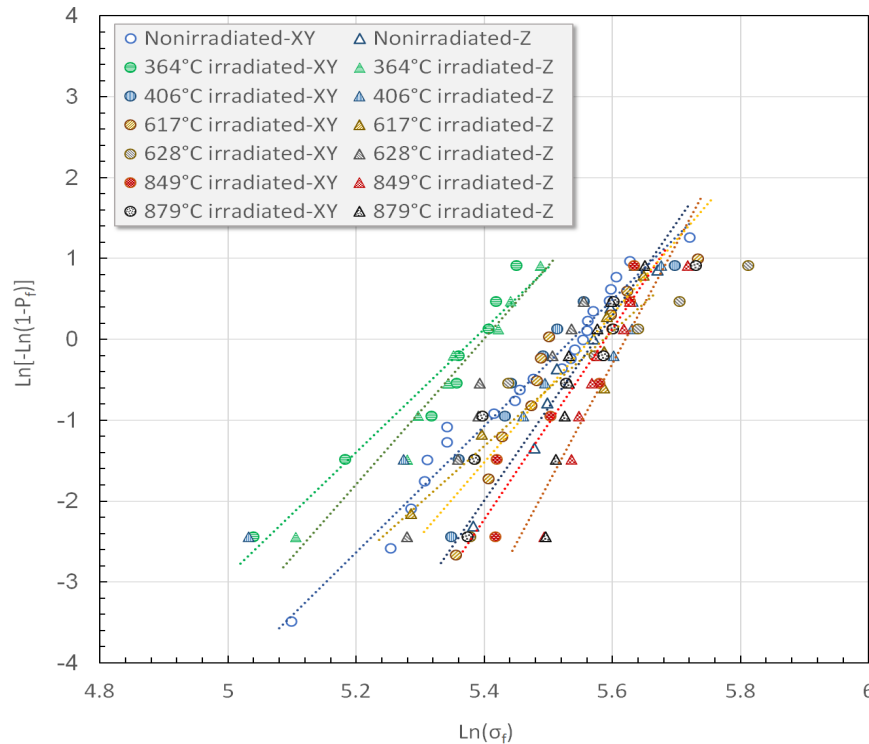


Figure 18. Weibull plot of strength as determined from equiaxial ring-on-ring tests of 3D-printed SiC disks with XY and Z orientations before and after irradiation to 2.3 dpa.

The key conclusion to be drawn from these results is that within the accuracy of the measurements, overall, there is no significant difference in failure strength between XY and Z disks or within each orientation before and after irradiation. However, careful comparison of the datasets shows some radiation effects when the irradiation temperature is below $\sim 400^\circ\text{C}$. The irradiation temperature of capsule SDTR04 was 364°C , and the two failure strength parameters—the mean and characteristic strength values—are $\sim 20\%$ lower than those of pre-irradiation values (see the data indicated in green in Fig. 18). This indicates that a slight embrittlement has progressed in these specimens during irradiation at the relatively low temperature. This may be the only noticeable change in strength level due to irradiation. The strength values from other irradiation temperatures are well within the range of statistical variations. Another radiation effect observed is that 3 out of 4 Weibull moduli that were measured after the highest temperature (849 and 879°C) irradiations are obviously higher than the others. This implies that some recovery of defects or mitigation of cracking sensitivity to initiation sites occurs during the high temperature irradiations. Besides these small changes, no other effects were noticed in this experiment. In

fact, the absence of any significant effect of irradiation on the strength of the disks is well documented as being characteristic of high purity and crystalline SiC [8].

Table 7. Characteristic strength and Weibull modulus determined for 3D-printed SiC at different orientations before and after irradiation. Note that these results are based on a limited number of tests (23 tests for nonirradiated and 8 (or 7) tests for irradiated specimen datasets).

Specimen orientation (→)	XY			Z		
Specimen condition	Weibull modulus (m)	Mean strength (MPa)	Characteristic strength (MPa)	Weibull modulus (m)	Mean strength (MPa)	Characteristic strength (MPa)
Nonirradiated	7.8	239	254	11.4	253	264
Irradiated at 364 °C (SDTR04)	7.6	205	218	9.0	210	221
Irradiated at 406 °C (SDTR01)	8.9	241	254	4.8	244	266
Irradiated at 617 °C (SDTR05)	9.2	248	261	7.0	251	267
Irradiated at 628 °C (SDTR02)	6.0	258	278	8.9	236	248
Irradiated at 849 °C (SDTR06)	11.8	257	268	14.8	267	276
Irradiated at 879 °C (SDTR03)	7.9	253	268	18.9	258	265
CVD SiC (nonirr.)	9.4	333	351			

5.2 THERMOPHYSICAL PROPERTIES

As described in Section 3.2.1, the thermal diffusivity data of nonirradiated SiC specimens were obtained using a Netzsch MicroFlash® LFA 457, which uses an Nd:Glass (1.06 mm) laser to deposit a short laser pulse to the front surface of the disks and an infrared detector to monitor the back surface temperature increase. Irradiated SiC samples were tested in the LAMDA lab using a Netzsch HyperFlash® LFA 467HT, which uses a xenon flash lamp to heat the sample surface. All specimens were 0.5 mm thick and 6 mm in diameter. Measurements were carried out in an argon environment with an argon purge rate of 100 ml/min. Diffusivity was measured starting at room temperature and then at 100°C increments during heating. Data measurements were also taken at 100, 300 and 600°C (when applicable) during cooling. During this PIE, care was taken not to heat the specimens beyond the capsule irradiation temperature to avoid annealing of irradiation defects [38]. Both flash diffusivity systems and data analysis were in accordance with ASTM 1461 [27] requirements.

Specific heat capacity (C_p) of unirradiated SiC was measured using a Netzsch Pegasus 404 F1 DSC [19]. The 3-run ratio method was used with a sapphire standard according to ASTM 1269 [32]. Measurements were performed using the same thermal diffusivity disks under helium purge gas at a heating rate of 20K/min. Thermal conductivity, k , was calculated using Eq. (10). It is assumed that the effect of neutron irradiation on the specific heat capacity is negligible because of the limited change in the density following irradiation.

The thermal conductivity of 3D-printed SiC in two different orientations before and after neutron irradiation is plotted in Fig. 19. As conspicuously shown in the nonirradiated state (see Fig. 11), the thermal conductivity is significantly lower in the XY disks than in the Z disks. This discrepancy in thermal conductivity associated with the different specimen orientation disappears almost entirely after irradiation to 2.3 dpa at various temperatures.

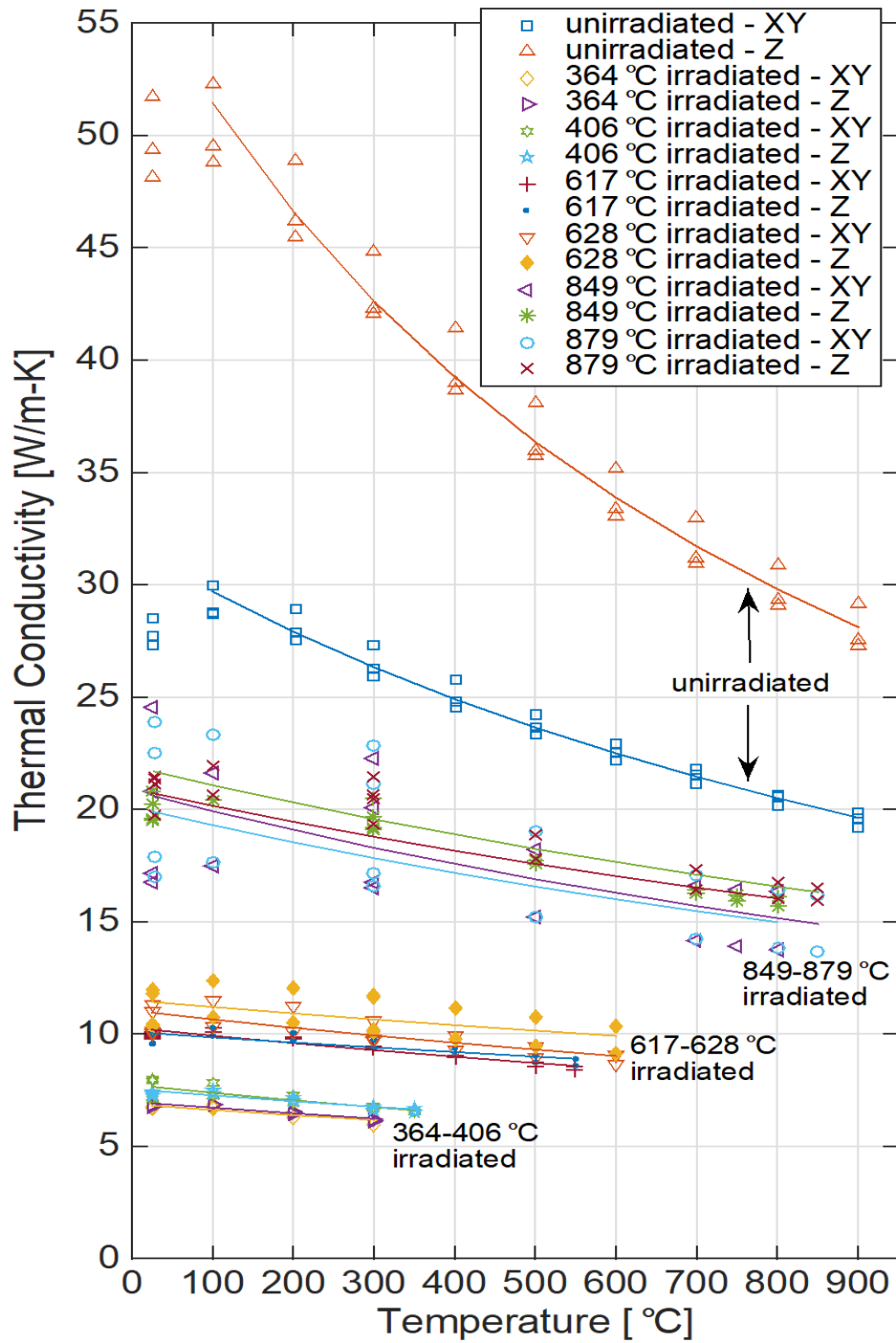


Figure 19. Thermal conductivity of 3D-printed SiC in the XY and Z orientations before and after irradiation to 2.3 dpa at various temperatures.

Thermal resistivity (R) is the inverse of thermal conductivity (k) and the sum of matrix, grain boundary, Umklapp, and irradiation defect resistivities (respectively, R_m , R_{gb} , R_U , R_d), as expressed in Eq. (12):

$$k^{-1} = R = R_m + R_{gb} + R_U + R_m + R_d, \quad (12)$$

Since no grain size evolution occurs after irradiation at these temperatures, and assuming that Umklapp scattering is unaffected by irradiation defects, the irradiation defect resistivity may be determined simply as the difference between specimen resistivity before and after irradiation.

$$R_d = R_{Irr} - R_{Unirr}, \quad (13)$$

The R_d for 3D-printed SiC is plotted in Fig. 20, along with those determined previously for CVD-SiC [8] and NITE-SiC [1]. As expected, the irradiation defect resistivities of these materials are very similar, as they all comprise primarily pure and crystalline SiC grains. Note that the calculated R_d for 3D-printed SiC appears to be lower than that of CVD-SiC at the highest irradiation temperature. This may be because the irradiation defects that scatter phonons have yet to reach full saturation in their size and number density at 2.3 dpa in this material [8]. Given that the unirradiated resistivity for the Z disks was lower and the post irradiation resistivity for the different orientations is similar, R_d appears to be higher for the Z disks.

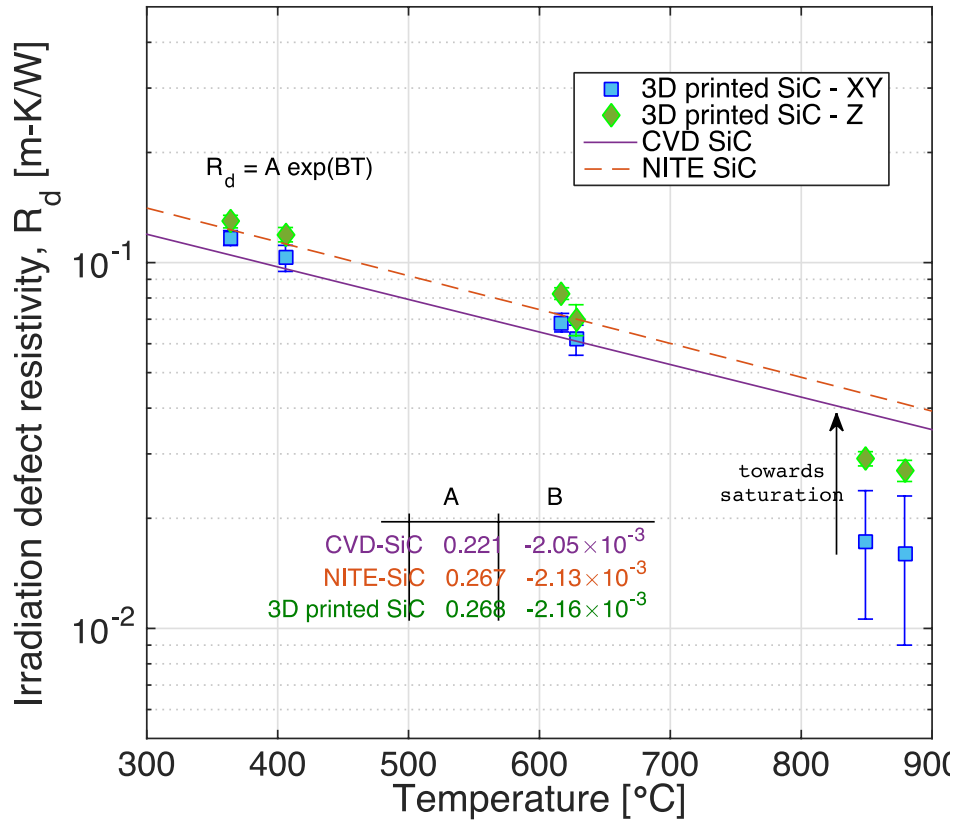


Figure 20. Irradiation defect resistivity, R_d , as a function of irradiation temperature for 3D-printed SiC, CVD-SiC [8], and NITE-SiC [1].

5.3 MICROSTRUCTURE AFTER IRRADIATION

5.3.1 Neutron Irradiation Effects

PIE by transmission electron microscopy (TEM) and scanning transmission electron microscopy (STEM) was carried out on the neutron-irradiated 3D-printed SiC obtained after irradiation to 2.3 dpa in HFIR at the target temperatures of 400, 650, and 900°C. Samples were prepared for TEM/STEM using standard dual-beam focused ion beam/scanning electron microscope (FIB/SEM) lift-out techniques on either an FEI Quanta 3D FIB/SEM or an FEI Versa 3D FIB/SEM; low energy ions were used for final thinning to reduce Ga-ion beam damage. TEM/STEM analysis was performed on an FEI Talos F200X STEM. Characterization was performed on samples from the XY and Z printed orientations. However, there was no meaningful difference between the two with respect to radiation effects and degree of radiation damage.

The STEM images in Fig. 21 highlight the boundary between the α -SiC particles and the CVI matrix after irradiation at each temperature. Starting with the α -SiC particles, the so-called *black spot damage*, which shows up in bright field (BF) imaging as dark black spots, approximately ~nanometer size, and/or dislocation loops, are visible in the α -SiC particles at all temperatures, though these are easier to see as bright spots in the annular dark field (ADF) images, particular in the 400°C sample. The black spots are easier to see at 650°C because they are slightly larger [2]. Whereas only black spot damage is observed in the α -SiC particles at 400 and 650°C, both black spot damage and 5–10 nm diameter dislocation loops are observed in the α -SiC particle at 900°C [2]. Moving toward the interface between the α -SiC particles and the CVI matrix, a black spot/ dislocation loop denuded zone is observable, particularly at 900°C, due to the strong contrast between the dislocation loops and the surrounding area. This denuded zone suggests the interface between the α -SiC particles and the CVI matrix is a sink for point defects. Lastly, in the CVI matrix, at 400 and 650°C, a small amount of potential radiation damage can be observed in the CVI region within about 50 nm of the interface, as there are signs of black spot damage. However, at 900°C, there is no damage shown near the interface. Within the bulk of CVI matrix at all temperatures, there is no observable difference between the irradiated samples and the unirradiated samples. There are two possible and perhaps related reasons for this that are not mutually exclusive: (1) the highly faulted nature of the CVI matrix makes it very difficult to achieve good imaging conditions, and (2) the high density of faults may act as sinks for defects, thus limiting any radiation damage.

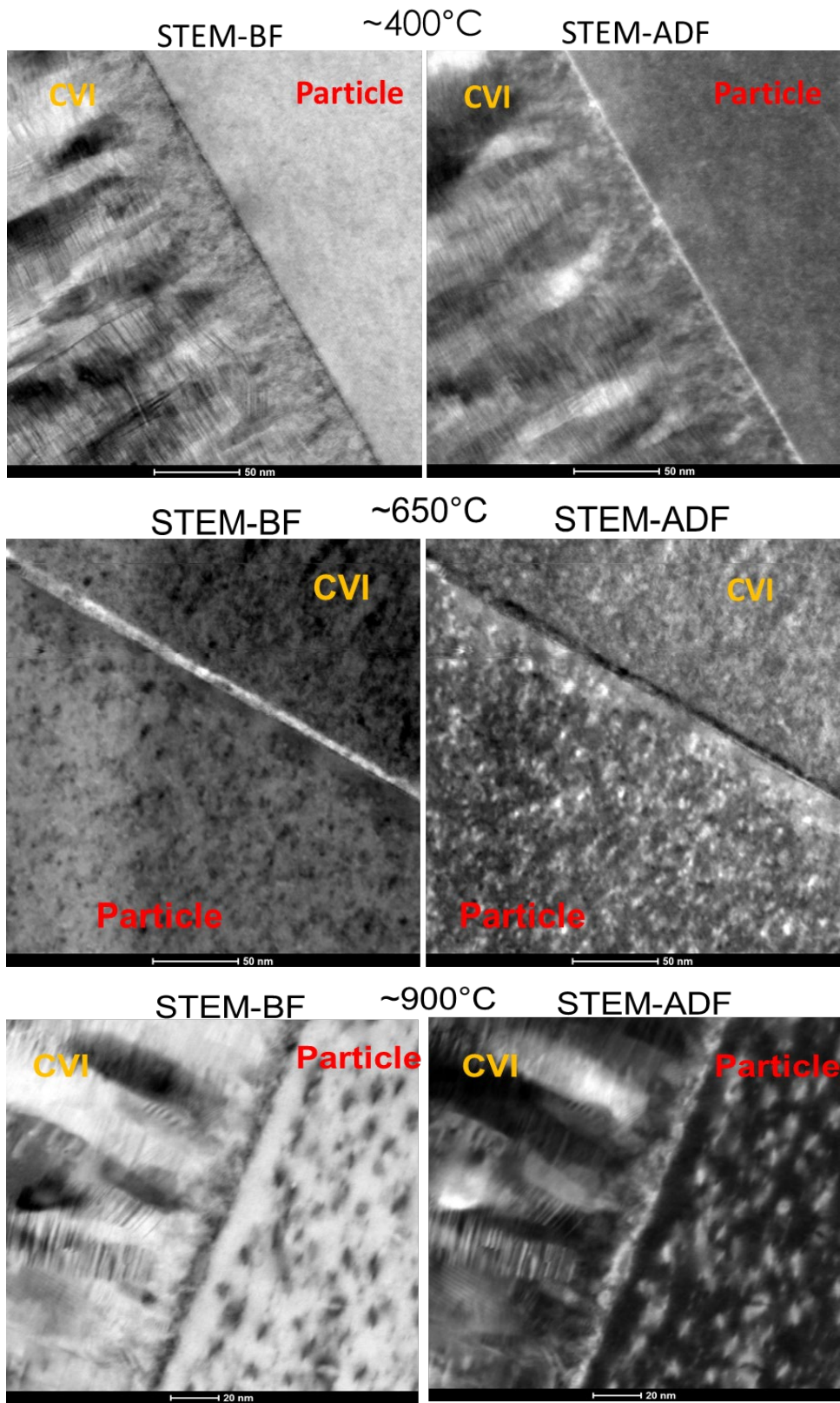


Figure 21. STEM BF and annular dark field images of the interface between the CVI matrix and the α -SiC particle after neutron irradiation in HFIR to a dose of 2.3 dpa at nominal temperatures of 400, 650, and 900°C

5.3.2 Ion Irradiation Effects

Ion irradiation was conducted at the Ion Beam Materials Laboratory at the University of Tennessee, Knoxville, to gain an understanding of radiation effects in the 3D-printed SiC at doses up to 40 dpa. The 3D-printed SiC samples were irradiated with 5 MeV Si²⁺ ions at two target temperatures of 350 and 650°C. In addition to the previous report, in which TEM and STEM imaging were used to characterize radiation-induced defects [19], additional microstructural characterization using STEM-based electron energy loss spectroscopy (EELS) was used to help quantify radiation damage in the CVI matrix relative to the α -SiC particles.

The ion-irradiated samples shown in Fig. 22 were irradiated at 350 and 650°C to peak doses of 40 dpa. This figure highlights many of the same features seen in the neutron-irradiated samples. However, the gradient in damage from the surface towards the peak damage depth enables some features to stand out more apparently than in the neutron-irradiated samples. Just as in the neutron-irradiated material, there is a high degree of black spot damage within the α -SiC particle and a lack visible damage within the CVI matrix. The black spot denuded zone is also apparent at the interface, as denoted by the green dotted arrows. Interestingly, the denuded zone increases in size at shallower depths/lower dose levels, especially in the 350°C sample. In the 650°C sample, black spot density appears to increase in the particle as the CVI interface is approached up until the denuded zone, as denoted by the blue dashed arrow parallel to the lamella surface. This illustrates that point defects are mobile and that the net flux changes based on temperature since the gradient is reversed in the lower temperature 350°C sample.

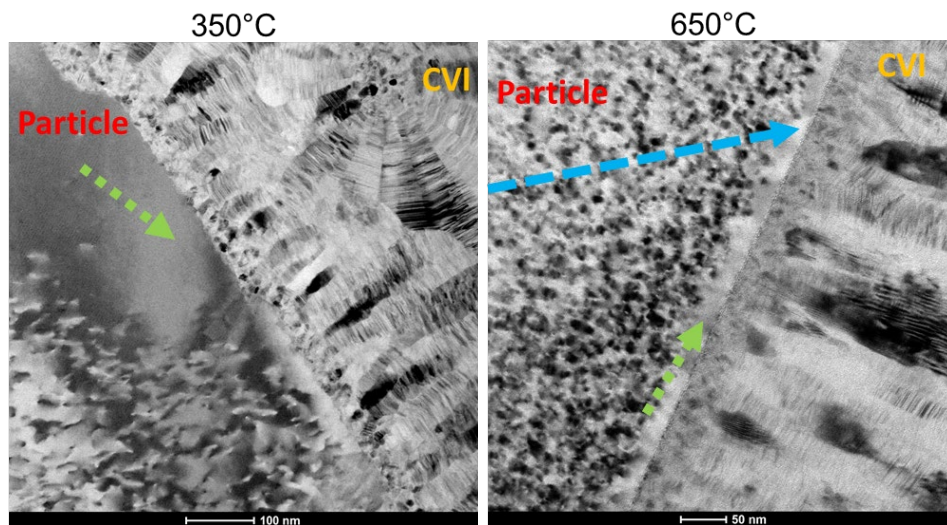


Figure 22. TEM BF images of the interface between the CVI matrix and α -SiC particles in the 5 MeV Si ion-irradiated specimens to a peak dose of 40 dpa at 350 and 650 °C. The blue dashed arrow is parallel to the lamella surface and highlights black spot damage relative to the position of the interface. The green dotted arrow highlights the black spot denuded zone near the interface.

The lack of visible defects in the CVI matrix may be the result of difficult imaging conditions. Another method must be used to observe and quantify radiation-induced defects. One possible solution is to use STEM-EELS analysis, in which the energy of the plasmon peak in the EELS spectra is relative to the zero-loss peak, as shown in Fig. 23(a). This energy difference in the EELS spectrum is proportional to the density of valence electrons; if atoms are missing, such as in the form of radiation-induced vacancies, then the density of valence electrons decreases, resulting in a red shift of plasmon peak to lower energies [39, 40]. Comparing the relative plasmon peak energy of the irradiated material with the unirradiated material can give an approximate degree of volumetric change, and thus swelling using Eq. (15) [39, 40]:

$$\text{Swelling fraction} = \left(\frac{eV_{U_{irr}}}{eV_{irr}}\right)^2 - 1 \quad (15)$$

Irradiation-induced vacancies lead to point defect swelling, as evidenced by plotting density change as a function of depth in the ion-irradiated samples, as shown in Fig. 23(b). However, the difference between the CVI matrix and the α -SiC particles is relatively small. The measured point defect swelling at each temperature is consistent with other forms of SiC: $\sim 2\text{--}3\%$ at 350°C , and $\sim 1\text{--}2\%$ at 650°C [2]. At both temperatures, the CVI matrix has slightly greater swelling than the particle, but the difference in swelling appears to be minor and could be due to complex behavior of the high density of intrinsic stacking faults in CVI. It could also be due to a potential bias in sink strength toward interstitials over vacancies, particularly as the difference in swelling is slightly more pronounced at the lower temperature, where vacancies are less mobile. Whether these small differences in defect swelling behavior are real, they could be accommodated by the grown-in porosity found within the CVI matrix, and they may be the result of incomplete densification. Post-irradiation, any difference in fracture strength or thermal diffusivity between the CVI matrix and the α -SiC particles is not readily apparent from Figures 18, 19, or 20; therefore, any difference in radiation damage between the CVI matrix and the α -SiC particles appears to be insignificant.

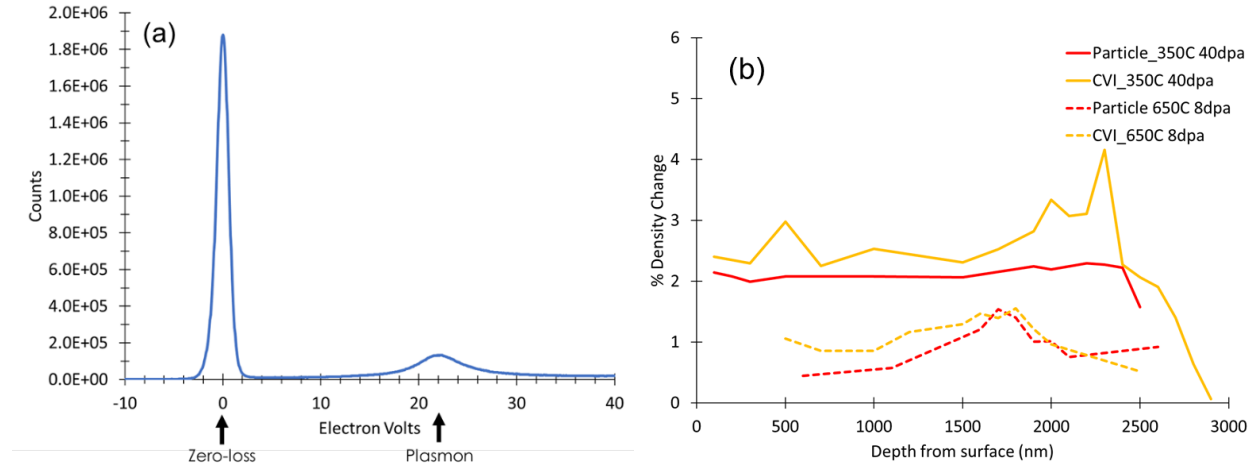


Figure 23. (a) Sample STEM-EELS spectrum highlighting position of plasmon peak relative to the zero-loss peak. (b) Measured density change using Eq. (15) as a function of depth in the α -SiC particle and CVI matrix in ion-irradiated samples at both temperatures.

6. SUMMARY AND CONCLUSIONS

Mechanical and thermophysical tests were carried out before and after neutron irradiation to evaluate the performance of SiC materials produced by a combined process of binderjet 3D printing and CVI. The 3D-printed SiC disk specimens were neutron-irradiated to 2.3 dpa at different temperatures, and their thermophysical and mechanical properties were evaluated in the LAMDA lab. Discussion in this document is focused on the effects of specimen orientation on the mechanical and thermophysical properties and the effects of neutron irradiation on the same properties. The key results and conclusions derived from the testing and evaluation work are summarized below.

- [1] Equibiaxial flexural strength data were measured for four different SiC materials consisting of three printed SiC materials and one CVD SiC. Although the mean failure strengths of the 3D-printed SiC were $\sim 25\%$ lower than those of the reference material, CVD SiC, these values were still high (> 280 MPa). The measured Weibull moduli were within the range of 7–14, which is typical for SiC materials, and there was no evidence of different failure modes between the binderjet + CVI–

processed SiC and the reference CVD SiC. Comparisons of the failure strength data obtained under different conditions indicate that the effect of specimen orientation on SiC strength is not significant, but the effects of specimen thickness and surface roughness are more noteworthy.

- [2] The thermophysical properties of 3D-printed SiC after CVI were measured in three principal directions on multiple specimens. The measurements showed that specific heat and thermal expansion data are not sensitive to the build orientation, and the data agree with observations made regarding the reference CVD SiC. However, thermal diffusivity is highly dependent on the specimen orientation and can be correlated to the anisotropic microstructures of the 3D-printed SiC. Measured densities and elastic constants did not show any noticeable orientation dependence, but they were relatively lower than the theoretical or CVD SiC values.
- [3] Post-irradiation properties in a temperature range within the point defect swelling regime in SiC (350–900°C) were evaluated and analyzed. The thermal conductivity measurements that showed anisotropy in thermal transport in the 3D-printed SiC materials mostly disappeared after defect accumulation in irradiation. The thermal conductivity after irradiation was significantly reduced from that of nonirradiated SiC materials; in general, irradiation at lower temperatures caused more reduction of thermal conductivity due to higher defect accumulation.
- [4] No significant loss of failure strength was observed in the 3D-printed SiC materials as a result of neutron irradiation. The only exception was the strength data after the lowest temperature (< 400°C) irradiation that showed slight (~20%) radiation-induced reduction, which was because of less effective annihilation of radiation-produced defects at such low temperature. Orientation dependencies in the failure strength of SiC and its statistical behavior were not noticeable.
- [5] Transmission electron microscopy showed defect accumulation in the form of black spot damage within the binderjet printed α -SiC, which consistent with results observed in reference CVD-SiC material. Defect denuded zones were observed in the binderjet-printed particles near the interface with CVI SiC. On the other hand, under the imaging conditions of this study, irradiation-induced defects were not readily observed in the CVI matrix with fine and highly faulted grains except in some regions near the boundaries with the binderjet particles.

7. REFERENCES

- [1] Y. Katoh, L.L. Snead, C.H. Henager, T. Nozawa, T. Hinoki, A. Iveković, S. Novak, S.M. Gonzalez de Vicente, "Current status and recent research achievements in SiC/SiC composites," *J. Nucl. Mater.*, 455 (2014) 387–397.
- [2] K.A. Terrani, C. Ang, L.L. Snead, Y. Katoh, "Irradiation stability and thermo-mechanical properties of NITE-SiC irradiated to 10 dpa," *J. Nucl. Mater.*, 499 (2018) 242–247.
- [3] L.L. Snead, Y. Katoh, T. Nozawa, "Radiation Effects in SiC and SiC–SiC," in *Compr. Nucl. Mater.*, R. Konings, Ed., Oxford, Elsevier, 2012, p. 215–240.
- [4] Y. Katoh, K. Ozawa, C. Shih, T. Nozawa, R.J. Shnavski, A. Hasegawa, L.L. Snead, "Continuous SiC fiber, CVI SiC matrix composites for nuclear applications: Properties and irradiation effects," *J. Nucl. Mater.*, 448 (2014) 448–476.
- [5] Y. Katoh, L. Snead, "Silicon carbide and its composites for nuclear applications—Historical overview," *J. Nucl. Mater.*, 526 (2019) 151849.
- [6] Y. Katoh, N. Hashimoto, S. Kondo, L.L. Snead, A. Kohyama, "Microstructural development in cubic silicon carbide during irradiation at elevated temperatures," *J. Nucl. Mater.*, 351 (2006) 228–240.
- [7] K.A. Terrani, B.C. Jolly, M.P. Trammell, G. Vasudevamurthy, D. Schappel, B. Ade, G.W. Helmreich, H. Wang, A. Marquiz Rossy, B.R. Betzler, A.T. Nelson, "Architecture and properties of TCR fuel form," *J. Nucl. Mater.*, 547 (2021) 152781.
- [8] S. Kondo, Y. Katoh, L.L. Snead, "Concentric ring on ring test for unirradiated and irradiated miniature SiC specimens," *J. Nucl. Mater.*, 417 (2011) 406–410.
- [9] L.L. Snead, T. Nozawa, Y. Katoh, T. S. Byun, S. Kondo, D.A. Petti, "Handbook of SiC properties for fuel performance modeling," *J. Nucl. Mater.*, 371 (2007) 329–377.
- [10] Y. Katoh, T. Koyanagi, J.L. McDuffee, L.L. Snead, K. Yueh, "Dimensional stability and anisotropy of SiC and SiC-based composites in transition swelling regime," *J. Nucl. Mater.*, 499 (2018) 471–479.
- [11] Y. Katoh, T. Nozawa, L.L. Snead, K. Ozawa, H. Tanigawa, "Stability of SiC and its composites at high neutron fluence," *J. Nucl. Mater.*, 417 (2011) 400–405.
- [12] T. Koyanagi, T. Nozawa, Y. Katoh, L.L. Snead, "Mechanical property degradation of high crystalline SiC fiber-reinforced SiC matrix composite neutron irradiated to ~100 displacements per atom," *J. Eur. Ceram. Soc.*, (2017).
- [13] C.H. Carter, R.F. Davis, J. Bentley, "Kinetics and Mechanisms of High-Temperature Creep in Silicon Carbide: I, Reaction-Bonded," *J. Am. Ceram. Soc.*, 67 (1984) 409–417.
- [14] T. Koyanagi, Y. Katoh, K. Ozawa, K. Shimoda, T. Hinoki, L.L. Snead, "Neutron-irradiation creep of silicon carbide materials beyond the initial transient," *J. Nucl. Mater.*, 478 (2016) 97–111.
- [15] T. Koyanagi, K. Terrani, T. Karlsen, V. Andersson, D. Sprouster, L. Ecker, Y. Katoh, "In-pile tensile creep of chemical vapor deposited silicon carbide at 300 °C," *J. Nucl. Mater.*, 521 (2019) 63–70.
- [16] S. Park, D.H. Lee, H.I. Ryoo, T.W. Lim, D.Y. Yang, D.P. Kim, "Fabrication of three-dimensional SiC ceramic microstructures with near-zero shrinkage via dual crosslinking induced stereolithography," *Chem. Commun.*, 32 (2009) 4880–4882.

- [17] Y. de Hazan, D. Penner, "SiC and SiOC ceramic articles produced by stereolithography of acrylate modified polycarbosilane systems," *J. Eur. Ceram. Soc.*, 37 (2017) 5205–5212.
- [18] L. Weisensel, N. Travitzky, H. Sieber, P. Greil, "Laminated object manufacturing (LOM) of SiSiC composites," *Adv. Eng. Mater.*, 6 (2004) 899–903.
- [19] A. Zocca, P. Lima, S. Diener, N. Katsikis, J. Günster, "Additive manufacturing of SiSiC by layerwise slurry deposition and binder jetting (LSD-print)," *J. Eur. Ceram. Soc.*, 39 (2019) 3527–3533.
- [20] I. Polozov, N. Razumov, D. Masaylo, A. Silin, Y. Lebedeva, A. Popovich, "Fabrication of Silicon Carbide Fiber-Reinforced Silicon Carbide Matrix Composites Using Binder Jetting Additive Manufacturing from Irregularly-Shaped and Spherical Powders," *Materials (Basel)*, 13 (2020) 1766.
- [21] T. Koyanagi, K. Terrani, S. Harrison, J. Liu, Y. Katoh, "Additive manufacturing of silicon carbide for nuclear applications," *J. Nucl. Mater.*, 543 (2021) 152577.
- [22] K. Terrani, B. Jolly, M. Trammell, "3D printing of high-purity silicon carbide," *J. Am. Ceram. Soc.*, 103 (2020) 1575–1581.
- [23] K.A. Terrani, J.O. Kiggans, C.M. Silva, C. Shih, Y. Katoh, L.L. Snead, "Progress on matrix SiC processing and properties for fully ceramic microencapsulated fuel form," *J. Nucl. Mater.*, 457 (2015) 9–17.
- [24] K.A. Terrani, J.O. Kiggans, Y. Katoh, K. Shimoda, F.C. Montgomery, B.L. Armstrong, C.M. Parish, T. Hinoki, J.D. Hunn, L.L. Snead, "Fabrication and characterization of fully ceramic microencapsulated fuels," *J. Nucl. Mater.*, 426 (2012) 268–276.
- [25] B.R. Betzler, B.J. Ade, A.J. Wysocki, P.K. Jain, P.C. Chesser, M.S. Greenwood, K.A. Terrani, "Transformational Challenge Reactor Preconceptual Core Design Studies," *Nucl. Eng. Des.*, 367 (2020) 110781.
- [26] T.S. Byun, B.E. Garrison, H. Wang, A. Trofimov, T.G. Lach, C.M. Parish, B.C. Jolly, M.D. Richardson, M. Trammell, A. Schumacher, G. Vasudevamurthy, T. Koyanagi, K.A. Terrani, "Mechanical and Thermophysical Properties of 3D-Printed SiC-FY20," M2TC-21OR0403022 (ORNL/SPR-2020/1545), Oak Ridge National Laboratory, 2020.
- [27] K.G. Field, J. Simpson, M.N. Gushev, H. Wang, M. Li, X. Zhang, X. Chen, T. Koyanagi, K. Kane, A. Marquez Rossy, M. Balooch, K.A. Terrani, "Handbook of advanced manufactured material properties from TCR structure builds at ORNL – FY19," M3CT-19OR06090121, Oak Ridge National Laboratory, 2019.
- [28] K.A. Terrani, T. Lach, H. Wang, A. Le Coq, K. Linton, C. Petrie, T. Koyanagi, T.S. Byun, "Irradiation stability and thermomechanical properties of 3D-printed SiC," *J. Nucl. Mater.*, 551 (2021) 152980.
- [29] P. Champlin, J. Burns, C. M. Petrie, X. Hu, K. D. Linton, R. Howard, K. A. Terrani, "Capsule and Specimen Geometries for HFIR Irradiation Testing Supporting the Transformational Challenge Reactor," M3CT-19OR06090120 (ORNL/TM-2019/1310), Oak Ridge National Laboratory, 2019.
- [30] W. Weibull, "A statistical distribution function of wide applicability," *J. Applied Mechanics*, 18 (3) (1951) 293–297.

- [31] ASTM C1499 – 09 (Reapproved 2013): Standard Test Method for Monotonic Equibiaxial Flexural Strength of Advanced Ceramics at Ambient Temperature, ASTM International, West Conshohocken, PA, 2009.
- [32] J.C. Fothergill, "Propability Paper," *IEEE Tran. on Elect. Insul.*, 25 (1990) 489-492.
- [33] S.G. Hong, T.S. Byun, R.A. Lowden, L.L. Snead, Y. Katoh, "Evaluation of the Fracture Strength for SiC Layers in the TRISO-coated Fuel Particle," *J. of the Amer. Ceramics. Soc.*, 90 (2007) 184-191.
- [34] T. S. Byun, E. Lara-Curzio, L. L. Snead, Y. Katoh, "Miniaturized Fracture Stress Tests for Thin-Walled Tubular SiC Specimens," *J. of Nucl. Mater.*, 367-370 (2007) 653-658.
- [35] ASTM E1461-13: Standard test method for thermal diffusivity by the flash method, ASTM International, West Conshohocken, PA , 2013.
- [36] W.J. Parker, R.J. Jenkins, C.P. Butler, and G.L. Abbott, "Flash Method of Determining Thermal Diffusivity, Heat Capacity, and Thermal Conductivity," *J. Appl. Phys.*, 32 (1961) 1679.
- [37] R.D. Cowan, "Pulse Method of Measuring Thermal Diffusivity at High Temperatures," *J. Applied Physics*, 34(4) (1963) 926-927.
- [38] L.M. Clark III, R.E. Taylor, "Radiation loss in the flash method for thermal diffusivity," *J. Applied Physics* , 46(2) (1975) 714-719.
- [39] Goldberg Yu., Levinshstein M.E., Rummyantsev S.L., "Properties of Advanced Semiconductor Materials GaN, AlN, SiC, BN, SiC, SiGe," New York, John Wiley & Sons, Inc., 2001, pp. 93-148.
- [40] ASTM E1269-11, Standard Test Method for Determining Specific Heat Capacity by Differential Scanning Calorimetry, ASTM International, West Conshohocken, PA, 2018.
- [41] Carly M. Donahue, Marcel C. Remillieux, Gyanender Singh, T.J. Ulrich, Robert J. Migliori, Tarik A. Saleh, "Measuring the elastic tensor of a monolithic SiC hollow cylinder with resonant ultrasound spectroscopy," *NDT & E International*, 101 (2019) 29-33.
- [42] G. Singh, T. Koyanagi, C. Petrie, C. Deck, K. Terrani, J.D. Arregui-Mena, Y. Katoh, "Elastic moduli reduction in SiC-SiC tubular specimen after high heat flux neutron irradiation measured by resonant ultrasound spectroscopy," *J. Nucl. Mater.*, 523 (2019) 391-401.
- [43] K.G. Field, J.L. McDuffee, J.W. Geringer, C.M. Petrie, Y. Katoh, "Evaluation of the continuous dilatometer method of silicon carbide thermometry for passive irradiation temperature determination," *Nucl. Instruments Methods Phys. Res. Sect. B: Beam Interact. with Mater. Atoms.*, 445 (2019) 46–56.
- [44] L.R. Greenwood, R.K. Smither, "SPECTER: Neutron Damage Calculations for Materials Irradiations," ANL/FPP/TM-197, Argonne National Laboratory, 1985.
- [45] L.L. Snead, K.A. Terrani, Y. Katoh, C. Silva, K.J. Leonard, A.G. Perez-Bergquist, "Stability of SiC-matrix microencapsulated fuel constituents at relevant LWR conditions," *J. Nucl. Mater.*, 448 (2014) 389–398.
- [46] I.T. Bae, W.J. Weber, Y. Zhang, "Direct measurement of local volume change in ion-irradiated and annealed SiC," *J. Appl. Phys.*, 106 (2009) 123525.

- [47] W. Jiang, C. M. Wang, W. J. Weber, M. H. Engelhard, L. V. Saraf, "Direct determination of volume changes in ion-beam-irradiated SiC," *J. Appl. Phys.*, 95 (2004) 4687.
- [48] J. Simpson, J. Haley, C. Cramer, O. Shafer, A. Elliott, W. Peter, L. Love, R. Dehoff, "Considerations for Application of Additive Manufacturing to Nuclear Reactor Core Components," M3CT-19OR06090123 (ORNL/TM-2019/1190), Oak Ridge National Laboratory, 2019.
- [49] ASTM E1461-07: Standard Test Method for Thermal Diffusivity by the Flash Method, ASTM International, West Conshohocken, PA, 2007.
- [50] S.J. Zinkle, L.L. Snead, "Designing radiation resistance in materials for fusion energy," *Annu. Rev. Mater. Res.*, 44 (2014) 241–267.
- [51] E.J. Opila, R.E. Hann, "Paralinear oxidation of CVD SiC in water vapor," *J. Am. Ceram. Soc.*, 80 (1997) 197–205.
- [52] K.A. Terrani, B.A. Pint, C.M. Parish, C.M. Silva, L.L. Snead, Y. Katoh, "Silicon carbide oxidation in steam up to 2 MPa," *J. Am. Ceram. Soc.*, 97 (2014) 13094.
- [53] P.A. Mouche, K.A. Terrani, " Steam pressure and velocity effects on high temperature silicon carbide oxidation," *J. Am. Ceram. Soc.*, 103 (2020) 2062–207.
- [54] K.A. Terrani, B.C. Jolly, M.P. Trammell, G. Vasadevamurthy, D. Schappel, B. Ade, G.W. Helmreich, H. Wang, A.M. Rossy, B.R. Betzler, A.T. Nelson, "Architecture and properties of TCR fuel form," *J. Nucl. Mater.*, 547 (2020) 152781.
- [55] L.L. Snead, S.J. Zinkle, D.P. White, "Thermal conductivity degradation of ceramic materials due to low temperature low dose neutron irradiation," *J. Nucl. Mater.*, 340 (2005) 187–202.
- [56] L. Jamison, M.-J. Zheng, S. Shannon, T. Allen, D. Morgan, I. Szlufarska, "Experimental and ab initio study of enhanced resistance to amorphization of nanocrystalline silicon carbide under electron irradiation," *J. Nucl. Mater.*, 445 (2014) 181–189.
- [57] L.L. Snead, Y. Katoh, T. Koyanagi, K. Terrani, E.D. Specht, "Dimensional isotropy of 6H and 3C SiC under neutron irradiation," *J. Nucl. Mater.*, 471 (2016) 92–96.
- [58] Y. Zhang, M. Ishimaru, T. Varga, T. Oda, C. Hardiman, H. Xue, Y. Katoh, S. Shannon, W.J. Weber, "Nanoscale engineering of radiation tolerant silicon carbide," *Phys. Chem. Chem. Phys.*, 14 (2012) 13429–13436.
- [59] M.P. Trammell, B.C. Jolly, M.D. Richardson, A.T. Schumacher, K.A. Terrani, "Advanced Nuclear Fuel Fabrication: Particle Fuel Concept for TCR," ORNL/SPR-2019/1216, Oak Ridge National Laboratory, 2019.
- [60] P.K. Fischer, G.A. Schneider, "Dielectric breakdown toughness from filament induced dielectric breakdown in borosilicate glass," *J. European Ceramic Soc.*, 38 (2018) 4476-4482.